International Journal of Quantum Chemistry

WILEY

International Journal of QUANTUM CHEMISTRY

RESEARCH ARTICLE OPEN ACCESS

Exploring the Therapeutic Potential of Cannabidiol in Cutaneous Squamous Cell Carcinoma: An Integrated Computational and Experimental Study

Andrea Jess Josiah[1,2] | Krishna Kuben Govender[2] | Penny Poomani Govender[2] | Werner Cordier[3] | Margo Nell[3] | Suprakas Sinha Ray[1,2]

[1]Centre for Nanostructured and Advanced Materials, DSI-CSIR Nanotechnology Innovation Centre, Council for Scientific and Industrial Research, Pretoria, South Africa | [2]Department of Chemical Sciences, University of Johannesburg, Johannesburg, South Africa | [3]Department of Pharmacology, University of Pretoria, Pretoria, South Africa

Correspondence: Krishna Kuben Govender (krishnag@uj.ac.za) | Suprakas Sinha Ray (rsuprakas@csir.co.za; ssinharay@uj.ac.za)

Received: 25 March 2025 | **Revised:** 19 December 2025 | **Accepted:** 17 February 2026

Keywords: cannabidiol | DFT | MM-GBSA | molecular docking | squamous cell carcinoma | SRB assay

ABSTRACT

Cutaneous squamous cell carcinoma (cSCC) poses a significant therapeutic challenge due to its aggressive nature and recurrence rates. The current treatment 5-fluorouracil (5-FU) is associated with adverse skin reactions. This study investigates cannabidiol (CBD) as a potential alternative therapy for cSCC through an integrated computational and experimental approach. Density functional theory (DFT) using the M06-2X/6-31+G(d,p) basis set revealed that CBD's smaller HOMO–LUMO gap (0.282 eV) compared to 5-FU (0.288 eV) indicates a higher reactivity and potential biological interactions. Cannabidiol exhibits a higher binding affinity toward the CB1 receptor (−9.986 kcal/mol) than 5-FU (−3.760 kcal/mol). Molecular dynamics simulations demonstrate that the CBD–CB1 complex remains stable through hydrogen bonding and hydrophobic interactions. Binding free energy calculations (MM-GBSA) further confirmed CBD's enhanced affinity (−69.696 kcal/mol) over 5-FU (−28.241 kcal/mol). Experimentally, CBD exhibited greater cytotoxicity against A431 cSCC cells with an IC_{50} of 2.76 μM compared to 5-FU's IC_{50} of 5.61 μM. These integrated findings suggest that CBD is a promising alternative therapeutic candidate for cSCC, offering superior cytotoxicity and stable molecular interactions compared to 5-FU.

1 | Introduction

Cancer represents a significant global healthcare challenge owing to its diverse nature, necessitating continuous innovation in treatment strategies [1]. In 2020, 10 million deaths were attributed to cancer [2], moreover, studies indicate that an excess of 24 million cancer cases will be diagnosed between 2020 and 2035 [3]. Among the multitude of malignancies, skin cancer emerges as one of the most prevalent, with 1.2 million new cases reported in 2020 [2]. Skin cancer is characterized by the unsuppressed proliferation of aberrant skin cells [4], delineating two principal categories: melanoma and nonmelanoma skin cancer (NMSC) [5]. A predominant variant of NMSC is keratinocyte carcinoma (KC), composed of two subtypes: basal cell carcinoma (BCC) and squamous cell carcinoma (SCC) [6]. BCC occurs in basal epidermal cells and has a low malignancy potential and limited metastatic capacity. In contrast, SCC is a proliferative invasive carcinoma that affects squamous epidermal cells, posing a higher risk of metastasis and high recurrence rates [7]. In addition, cutaneous squamous cell carcinoma (cSCC) ranks as the second most prevalent variant of skin cancer. An estimated 1.8 million cases of cSCC are diagnosed annually in the United States [8]. Furthermore, an increased risk

of mortality is linked to advanced cSCC. A study by Karia et al. [9], 2013 revealed that cSCC mortality rates in the central and southern US have risen to levels comparable to melanoma.

The principal risk factor for cSCC development is prolonged exposure to ultraviolet radiation (UVA and UVB), which leads to DNA mutations in pro-oncogenes or tumor suppressor genes [10]. This carcinoma develops from precursor lesions, which include squamous cell carcinoma in situ (SCCIS) and actinic keratoses [11]. The development of cSCC is multifactorial, involving immune regulation, genetic mutations, and cellular mechanisms. There are two primary mechanisms contributing to the immunoregulatory processes in cSCC. First, elevated levels of transforming growth factor-beta (TGF-β), interleukin-10 (IL-10), and regulatory T cells (Tregs) in the tumor microenvironment (TME) of advanced cSCC. The increase in Tregs results in a suppressed antitumor immune system, which facilitates tumor progression [12]. Second, decreased plasmacytoid dendritic cells (pDCs) [13], lead to diminished activation of immune responses against the tumor [14]. Additionally, genomic sequencing in cSCC reveals that mutations in key genes, including Notch receptors 1 and 2 (NOTCH1/2), cyclin-dependent kinase inhibitor 2A (CDKN2A), Harvey rat sarcoma viral oncogene homolog (HRAS), tumor protein p53 (TP53), and transforming growth factor-beta receptor 1 (TGFBR1), drive early tumorigenesis through sustained clonal proliferation [15–19]. Epithelial–mesenchymal transition (EMT), influenced by the plasticity of tumor cells, is a cellular mechanism involved in both multidrug resistance and metastatic potential [20]. These interrelated factors highlight the complexity of cSCC pathogenesis and the necessity for therapeutic strategies that address multiple facets of the disease.

Currently, the pharmaceutical industry offers several topical treatments for cSCC, such as Ingenol mebutate, 5-fluorouracil (5-FU), and imiquimod. However, these treatments often lead to adverse skin reactions and recurrence. 5-FU, in particular, commonly causes pain, crusting, pruritus, erythema, and eczematous reactions, with localized irritation potentially progressing to ulceration and infection risk [21–23]. Despite 5-FU's historical role in treating cutaneous malignancies since 1957, its adverse effects highlight the critical need for alternative treatments.

Cannabinoids are bioactive compounds classified into phytocannabinoids, endocannabinoids, and synthetic cannabinoids [24]. Cannabidiol (CBD; IUPAC name 2-[(1R,6R)-3-methyl-6-(prop-1-en-2-yl)cyclohex-2-en-1-yl]-5-pentylbenzene-1,3-diol) is one of the predominant phytocannabinoids present in Cannabis, which is part of the Cannabaceae family. Cannabis is an herbaceous species that originates from Central Asia and is reported to produce more than 750 natural components of different chemical classes [25]. The World Health Organization (WHO) described CBD as a 21-carbon atom terpenophenolic compound [26]. The skin contains an endocannabinoid system (ECS) that plays a role in homeostasis by functioning as a signaling network. The ECS also contributes to various physiological processes, including inflammation, cellular growth, and immune response [27]. This system consists of endocannabinoid receptors, endogenous agonists, and enzymes [28]. The principal endocannabinoids, anandamide (AEA), and 2-arachidonoylglycerol (2-AG), function as natural ligands for both cannabinoid receptors 1 (CB1R) and 2 (CB2R) [29]. Both CB1R and CB2R are variably expressed in sebocytes, fibroblasts, cutaneous nerves, and keratinocytes [30]. Fatty acid amide hydrolase (FAAH) and monoacylglycerol lipase (MAGL) are enzymes that facilitate the synthesis and degradation of natural endocannabinoids [27].

Cannabidiol exhibits a range of biological properties that contribute to its therapeutic potential. As a phenolic compound, CBD is widely used in treating various diseases due to enhanced antioxidant activity, as reported by Amini and Akbari [31]. Kassim et al. [32] further indicated that certain phenolic acids, derived from phenolic compounds and containing at least one carboxylic group, exhibit antioxidant, anticancer, and anti-inflammatory properties. A study by Gohad et al. investigated the antioxidant properties of CBD on keratinocytes and melanocytes exposed to UV radiation. The research concluded that CBD demonstrated antioxidant effects, as evidenced by a reduction in cell death among these skin cells [33]. Additionally, a preclinical study demonstrated that CBD inhibits cell proliferation in Kaposi's sarcoma cells [34], highlighting its anticancer capabilities. Previous studies on CBD's therapeutic effects highlight that CBD modulates several signaling pathways including PI3K/AKT/mTOR, MAPK/ERK, and NF-κB, which result in cell growth inhibition, apoptosis, and tumor angiogenesis suppression. Moreover, in head and neck SCC's, CBD induces apoptotic and autophagic processes [35]. These processes decrease tumor growth and proliferation by upregulating dual specificity phosphatase 1 (DUSP1). The DUSP1 inactivates oncogenic MAPK isoforms, disrupting signaling cascades required for tumor cell survival and expansion [36].

Within the field of drug design, the efficacy of a drug is determined by its molecular recognition of a biological target, driven by the spatial and electronic characteristics of the drug's atoms [37]. Theoretical chemistry integrates mathematical methods with principles of quantum or classical mechanics, forming a strategic approach for analyzing and understanding chemical systems [38]. Computational chemistry emerges as a subdiscipline that applies theoretical chemical concepts via software tools [39]. Two integral components in computational chemistry include quantum mechanics (QM) and molecular mechanics (MM) calculations, which are employed to analyze and predict the molecular structure and behavior of chemical compounds [40]. Density functional theory (DFT) is a leading quantum chemistry method due to the balance of accuracy and computational efficiency [41].

Employing DFT with the M06-2X functional and the 6-31+G(d,p) basis set provides several advantages. The computational efficiency of DFT enables its application to large complex biological systems [42]. Additionally, this method provides atomic-level insights for designing efficient drug delivery systems by analyzing interactions among drugs, polymers, and biomolecules, potentially avoiding extensive experimental trials [43]. When executed with the M06-2X functional, DFT calculations enhanced precision in simulating biomolecular characteristics, including noncovalent interactions, hydrogen bonding, and transition metal chemistry [44]. The M06-2X functional incorporates 54% Hartree–Fock exchange, approximately double the exchange fraction used in the M06 functional (27%), and is specifically

parameterized for main-group elements (nonmetals). This characteristic enhances its reliability in describing thermochemical, kinetic, and noncovalent interactions [45]. The 6-31+G(d,p) basis set represents a split-valence double-zeta basis set that includes additional diffuse and polarization functions. These characteristics enhance the flexibility and precision of molecular orbital representations [46, 47]. Moreover, this basis set balances accuracy and computational cost for various biomolecular applications [48].

This study explores CBD as a potential treatment for cSCC, due to its diverse biological properties, and its capacity to influence signaling pathways involved in tumor progression, apoptosis, and angiogenesis. As a naturally occurring plant bioactive, CBD offers a distinct advantage in sustainability and accessibility, aligning with the increasing interest in plant-based therapeutic strategies for cancer treatment. The study integrates three key disciplines: computational chemistry, experimental validation, and biological evaluation. By employing DFT with the M06-2X/6-31+G(d,p) functional, the study investigates molecular geometry, electronic properties, and reactivity of CBD and 5-FU. Molecular docking and Molecular dynamics simulation (MDS) evaluate binding affinities and ligand stability within receptor active sites. Experimentally, FTIR and UV–vis spectroscopy validate theoretical predictions of molecular behavior, while cytotoxic assays assess CBD's efficacy in reducing cell viability in A431 SCC cells. Through this multidisciplinary approach, the study aims to establish a detailed understanding of CBD's molecular interaction and its potential as an anticancer therapy for cSCC.

2 | Materials and Methods

2.1 | Software

Quantum mechanical computations were performed using Gaussian 16 revision C01 [49] and GaussView 6.1 [50]. Gaussian 16 facilitated detailed quantum calculations, while GaussView 6.1 served as the graphical interface. Classical mechanics calculations were performed using the Schrödinger Maestro interface [51]. Physicochemical properties, pharmacokinetics, and drug-likeness analyses were conducted by SWISS-ADME [52]. Potential energy distribution (PED) was calculated by vibrational energy distribution analysis (VEDA) [53] and Fukui functions were determined by Multiwfn [54].

2.2 | Hardware

This study utilized the LENGAU high-performance computing cluster at the Centre for High-Performance Computing (CHPC) in Cape Town, South Africa [55].

2.3 | Acquisition and Preprocessing of Receptor Proteins and Ligands

Potential receptor targets for CBD interaction were identified through a literature survey, their three-dimensional (3D) structures were retrieved from the RCSB Protein Data Bank [56]. Additionally, the 3D structures of CBD (CID: 644019) and 5-FU (CID: 3385) were obtained from the PubChem database [57].

2.4 | DFT

The molecular characteristics of the CBD and 5-FU molecules were analyzed in Gaussian 16 using M06-2X/6-31+G(d,p). Geometry [58] optimization and vibrational frequency [59] analyses were performed to determine stable molecular structures and the corresponding vibrational modes. Electronic properties and reactivity were calculated by highest occupied molecular orbital (HOMO) and lowest unoccupied molecular orbital (LUMO) energy levels. Electrostatic potential (ESP) maps visualized charge distribution for potential interactions [49]. Fukui functions determined the reactivity [54], Ultraviolet–visible (UV) spectroscopy examined electronic transitions [60], which were simulated by time-dependent (TD)-DFT/M062X. Fourier-transform infrared (FTIR) spectroscopy identified functional groups and molecular vibrations [49]. Computational vibrational mode assignments were validated by VEDA. Gaussian calculations were performed in both the gas phase and dimethyl sulfoxide (DMSO) using the Integral Equation Formalism Polarizable Continuum Model (IEFPCM) as the implicit solvation model. However, only results from DMSO are reported, aligning with the experimental conditions.

2.5 | Molecular Docking

The 3D crystal structures of receptor proteins were prepared for docking using the Protein Preparation Wizard [61] tool in Schrödinger Maestro. Hydrogen bond optimization was performed at pH 7 using the PROPKA [62] tool, followed by structure minimization using the optimized potentials for liquid simulations—model 4 (OPLS4) force field [63]. The M06-2X/6-31+G(d,p) optimized CBD and 5-FU molecules were imported from Gaussian. Grid generation was performed using the receptor grid generation tool (within Schrödinger Maestro). Molecular docking was conducted with Glide XP [64, 65] (extra precision), using the OPLS4 force field [66].

2.6 | Molecular Dynamics Simulation Analysis

Molecular dynamics simulations (MDS) were performed on the docked complexes of CBD and 5-FU with the receptor that exhibited the highest binding affinity toward CBD. The protein–ligand complexes were prepared with the System Builder tool and solvated using the TIP4P water model within an orthorhombic periodic boundary box with a 10 Å buffer in all directions. To neutralize the system and mimic physiological conditions, a salt concentration of 0.15 M of NaCl was added. The MDS ran for 250 ns. The Molecular Mechanics-Generalized Born Surface Area (MM-GBSA) method [67] was employed to calculate the binding energies for the docked complexes of CBD and 5-FU. The strength of the interaction between proteins and ligands is quantified by the binding free energy (ΔG_{bind}), described in Equation (1). The ΔG_{bind} is calculated by summing several energetic contributions, as shown in Equation (2), where ΔE_{vdW} and ΔE_{ele} represent the van der Waals and Coulombic energies, respectively. The terms ΔE_{GB}, ΔE_{SA}, and $T\Delta S$ denote the

generalized Born electrostatic energy, nonpolar solvation energy, and conformational entropy change, respectively [68].

$$\Delta G_{\text{bind}} = G_{\text{complex}} - G_{\text{protein}} - G_{\text{ligand}} \quad (1)$$

$$\Delta G_{\text{bind}} = \Delta E_{\text{vdW}} + \Delta E_{\text{ele}} + \Delta E_{\text{GB}} + \Delta E_{\text{SA}} - T\Delta S \quad (2)$$

2.7 | Physiochemical and Pharmacokinetic Evaluation

Swiss ADME was used to comparatively evaluate the physicochemical properties, pharmacokinetics, and drug-likeness of CBD and 5-FU, with data sourced from PubChem [52].

2.8 | Target Prediction Analysis

Swiss target prediction was utilized to identify potential molecular targets for CBD. The CBD data was obtained from PubChem [69].

2.9 | Experimental

The CBD crystals used in this study had a purity of 99% (Endoca BV, Netherlands) and were kindly supplied by Tautomer Biosciences, South Africa. The 5-FU 99% was obtained from Sisco Research Laboratories, India (15088).

2.10 | Material Characterization

A Spectrum 100 FTIR spectrometer (PerkinElmer, USA) was employed to obtain the attenuated total reflectance Fourier transform infrared (ATR-FTIR) spectra for samples over a wavenumber range 4000–500 cm^{-1}, with a spectral resolution of 4 cm^{-1}, and 32 scans per spectrum. The UV–vis analysis was conducted using a UV5 UV/VIS Spectrophotometer (Mettler Toledo, UK), across a wavelength range from 200 to 800 nm. All samples were diluted in DMSO before analyses.

2.11 | Materials for Cytotoxic Assessment

The materials employed for assessing the cytotoxicity of CBD and 5-FU in SCC cells include: SCC cell line (A431; American Type Culture Collection); CBD (Endoca BV, Netherlands); 5-FU (Sisco Research Laboratories, India); Dulbecco's modified Eagle's medium (DMEM), fetal bovine serum (FBS), and phosphate-buffered saline (PBS) (Gibco—ThermoFisher Scientific, South Africa); acetic acid, dimethyl sulfoxide (DMSO), ethylenediaminetetraacetic acid (EDTA), penicillin, sodium hydroxide (NaOH), streptomycin, sulforhodamine B salt, trichloroacetic acid (TCA), trisaminomethane (Tris), trypan blue, and trypsin (Sigma-Aldrich, South Africa).

2.12 | Cell Culture

The A431 cells were cultured in 75 cm^2 culture flasks with DMEM, 10% heat-inactivated FBS, and 1% antibiotics (100 U/mL penicillin and 100 μg/mL streptomycin) at 37°C in a humidified incubator with 5% CO_2. Cells were subcultured upon reaching 70%–80% confluence. After rinsing with PBS, cells were detached using trypsin–EDTA (0.25% trypsin, 0.01% EDTA) for 10 min. Trypsin was deactivated using a complete medium, and cells were harvested via centrifugation at 200 RCF for 5 min. After the supernatant was discarded, the cell pellet was resuspended in 1 mL of 10% FBS-supplemented medium, and an aliquot thereof diluted with 0.1% trypan blue. Trypan blue-stained cells were counted with a hemocytometer, and the final cell concentration was adjusted to 100 000 cells/mL.

2.13 | Sulforhodamine B Staining

The A431 cells (100 μL) were seeded into a 96-well microtiter plate and incubated for 24 h at 37°C with 5% CO_2 to facilitate cell attachment. Cells were then treated for 48 h with 100 μL of either unsupplemented DMEM (negative control), 0.8% DMSO (vehicle control), 5-FU (2.2–35 μM; positive control), or CBD (2.2–35 μM) in FBS-free medium supplemented with 0.8% DMSO. Blanks containing 5% FBS-supplemented medium were included to account for sterility and background noise. Following treatment, cells were fixed with 50 μL of 50% TCA at 4°C for 24 h, washed with tap water, and air-dried. Subsequently, 100 μL of SRB dye (0.057% in 1% acetic acid) was added and incubated for 1 h. The unbound dye was removed with 100 μL of 1% acetic acid, plates were dried, and the bound dye was solubilized with 200 μL of 10 mM Tris buffer (pH 10.5). Plates were measured spectrophotometrically using an ELX 800 plate reader (BioTek Industries) at 540 nm with a reference wavelength of 630 nm. Values were blank-excluded, and the cell density was calculated using the following formula:

$$\text{Cell density (\%of negative control)} = \left(\frac{\text{absorbance of sample}}{\text{average absorbance of negative control}} \right) \times 100 \quad (3)$$

The assay was performed with technical and biological triplicates. GraphPad Prism software was employed for statistical analysis of the half-maximal inhibitory concentration (IC_{50}) [70], by plotting the logarithmic concentration relative to the cell density. A logarithmic normalized variable slope analysis was employed to determine the dose–response fit, where the IC_{50} was calculated based on the 50% cell density absolute value.

3 | Results and Discussion

3.1 | Molecular Geometry Optimization

Geometry optimization was performed to obtain a stable local minimum on the potential energy surface (PES) by minimizing the total energy. This initial step in QM analysis is essential, as its output constitutes the requisite input for all subsequent calculations [71]. Figure 1 illustrates the optimized geometry of the CBD and 5-FU molecules using M06-2X/6-31+G(d,p). Tables S1 and S2 display the optimized molecular geometry of each atom, specifying XYZ coordinates for CBD and 5-FU, respectively. Tables S3 and S4 represent a detailed analysis of the optimized bond lengths, bond angles, and dihedral angles of CBD and 5-FU. The CBD molecule demonstrates average

bond lengths of 1.3674, 0.9687, 1.4717, and 1.0947 Å, for O–C, O–H, C–C, and C–H, respectively. The bond angle data for CBD shows standard geometries for C–O–H (110.2915°), C–C–C (117.2852°), C–C–H (111.2097°). However, ring strain is observed at C4–C3–C5 (109.5512°) and a deviation at H39–C18–H40 (107.0025°), suggesting possible steric effects. The torsion angle data for CBD reveals conformational variability, with deviations at H47–O1–C11–C8 (−16.3661°), reflecting flexibility and potential steric interactions. The 5-FU molecular structure exhibits planarity in regions surrounding N4, N5, and C6 to C9, promoting electron delocalization and enhances stability, typical of aromatic systems [72]. Bond lengths of O2–C6 (1.2096 Å) and O3–C7 (1.2122 Å) indicate two carbonyl functional groups. Additionally, the N5–C7 (1.3833 Å) and N5–C9 (1.3795 Å) bond lengths suggest resonance or conjugation, further supporting electron delocalization. Bond angles C6–N4–C7 (128.5263°) and C7–N5–C9 (123.7488°) indicate sp^2 hybridization, which supports planarity. Electron-withdrawing groups fluorine (F1) and carbonyl oxygens (O2 and O3) alter the molecule's electronic environment. This is observed in the F1–C8 bond length (1.3342 Å), which suggests an inductive effect that minimally modifies adjacent bond angles. Torsion angles C7–N4–C6–O2 (−180.0027°) and F1–C8–C9–N5 (180.0055°) suggest a trans conformation, which minimizes steric repulsion and enhances planarity in aromatic systems.

3.2 | Fukui Functions

The Fukui function characterizes the change in electronic density that occurs due to a variation in the number of electrons while maintaining a constant external potential [73]. The Fukui function analysis of CBD and 5-FU reveals reactivity patterns defined by structural differences (Tables S5 and S6). Cannabidiol displays a balanced reactivity profile, with C17 as a primary electrophilic site ($\Delta f = -0.1117$) and C15 and C7 as nucleophilic centers. The O1 and O2 exhibit increased fr-values, reflecting electron-withdrawing behavior and susceptibility to nucleophilic attack. Furthermore, CBD maintains an evenly distributed electron density and a moderate Gibbs free energy change ($\Delta G = -15.6$ kJ/mol) obtained from DFT thermochemical analysis, supporting stability and broad interaction potential. Conversely, 5-FU displays increased reactivity, with C6 and C9 as nucleophilic sites and N5 and O3 as electrophilic. The

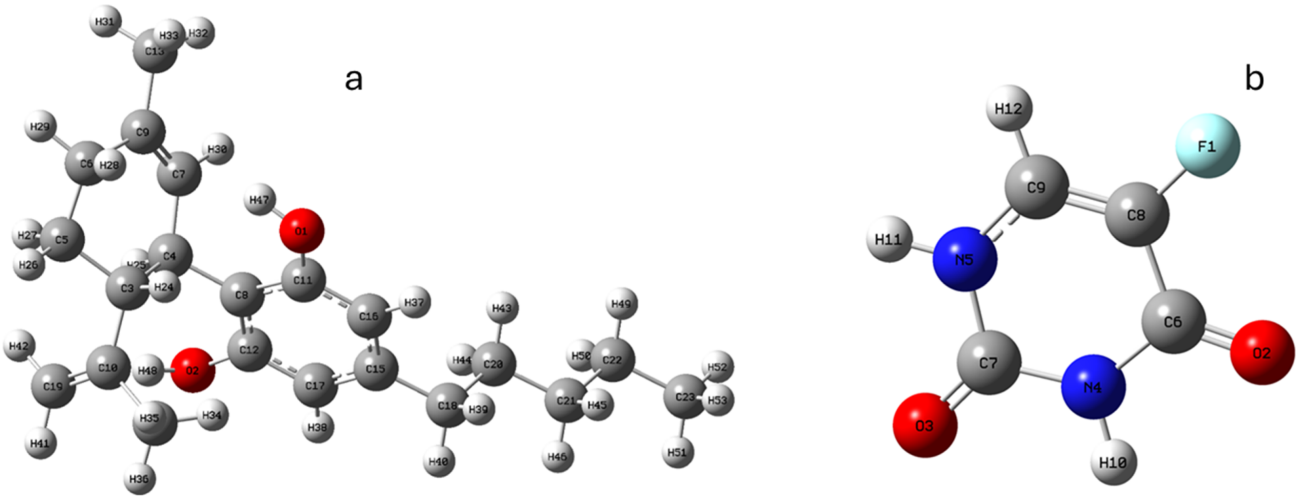

FIGURE 1 | Optimized molecular geometry of (a) cannabidiol and (b) 5-fluorouracil.

TABLE 1 | Comparative calculated energy values for cannabidiol and 5-fluorouracil using M06-2X/6-31+G(d,p).

Parameter	Symbol and formula	CBD	5-FU
HOMO energy (eV)	E_H	−0.2759	−0.3168
LUMO energy (eV)	E_L	0.0064	0.0290
$\Delta E_{HOMO-LUMO}$ gap (eV)	$\Delta E_G = E_L - E_H$	0.2824	0.2878
Ionization potential (eV)	$I = -E_H$	0.2759	0.3168
Electron affinity (eV)	$E_A = -E_L$	−0.0064	−0.0290
Global hardness (eV)	$\eta = (E_L - E_H)/2$	0.1412	0.1439
Chemical reactivity (eV^{-1})	$S = 1/\eta$	70 817	6.9493
Chemical potential	$\mu = (E_L + E_H)/2$	−0.1348	−0.3459
Electrophilicity index (eV)	$\omega = \mu^2/2\eta$	0.0643	0.0083
Electronegativity (eV)	$\chi = -\mu$	0.1348	0.3459
Dipole moment (Debye)	D	3.9429	4.1749

presence of F1 intensifies localized electrophilicity, supported by a higher ΔG of −27.3 kJ/mol, indicating stronger localized interactions.

3.3 | Frontier Molecular Orbitals (FMOs)

FMOs, predominately the HOMO and LUMO, are critical for predicting chemical reactivity and identifying interaction sites within a molecule. The HOMO–LUMO gap is an indicator of reactivity and stability, with a smaller gap associated with increased reactivity [74]. Table 1 and Figure 2 reveal the orbital characteristics of CBD and 5-FU. Delocalized electron density observed in the HOMO and LUMO across aromatic rings and oxygen substituents confirms enhanced resonance stability. This indicates potential reactivity through π–π stacking interactions or electron-sharing mechanisms [75]. 5-FU exhibits localized electron density around nitrogen and oxygen atoms in both the HOMO and LUMO. This reflects a higher electron affinity and electronegativity compared to CBD and indicates a greater electron-accepting ability that facilitates hydrogen bonding or nucleophilic attack. The smaller HOMO–LUMO gaps observed in both CBD (0.28241 eV) and 5-FU (0.2878 eV) indicate reactivity. However, CBD's slightly lower gap and higher chemical reactivity index (7.08165 eV^{-1} vs. 6.94927 eV^{-1}) indicate that CBD may have a broader range of reactivity. In addition, CBD's lower ionization potential (0.27599 eV) compared to 5-FU (0.31689 eV), highlights CBD's role as an electron donor. The comparative FMO analyses of CBD and 5-FU, elucidate the role of electron density and distribution influence biological activity. In CBD, the delocalized HOMO and LUMO facilitates interactions with diverse biological targets, enhancing its therapeutic versatility. Whereas 5-FU's localized electron density and higher electron affinity promote targeted electron-accepting interactions.

3.4 | Molecular Electrostatic Potential (MEP) Analysis

The determination of reactive atomic charges is essential for the application of quantum chemical calculations to molecular systems [76]. Figure 3 illustrates the ESP on the molecular surfaces of CBD and 5-FU, with color gradients representing variations in nucleophilic and electrophilic tendencies. Blue regions indicate stronger nucleophilic potential, while red regions denote a higher electrophilic potential. The electrical potential follows a decreasing order from blue (most nucleophilic) to red (most electrophilic): blue < cyan < orange < red. The moderate ESP range of CBD (−5.085e−2 to +5.085e−2) is associated with a balanced charge distribution. Nucleophilic regions are observed around oxygen atoms, which play a role in hydrogen bonding. Electrophilic regions correspond to hydrogen atoms in (−OH) groups and within the aromatic ring near the oxygen atoms. The observed neutral potential indicates structural stability, supporting broader but less intense biological interactions. 5-FU displays a wider ESP range (−8.199e−2 to +8.199e−2), with distinct nucleophilic and electrophilic regions. This polarization enhances 5-FU's reactivity and promotes strong polar interactions.

3.5 | Vibrational Spectral Analysis

Figure 4 presents a comparison between experimental FTIR wavenumbers and theoretical values calculated using the M06-2X/6-31+G(d,p) method, with a scaling factor of 0.952 applied (Table 2) [77]. The scaling factor was obtained from the Computational Chemistry Comparison and Benchmark Database (CCCBDB) to enhance the accuracy of the calculated vibrational frequencies with the experimental data. The O–H stretch in alcohols displays an experimental value of 3519 cm^{-1},

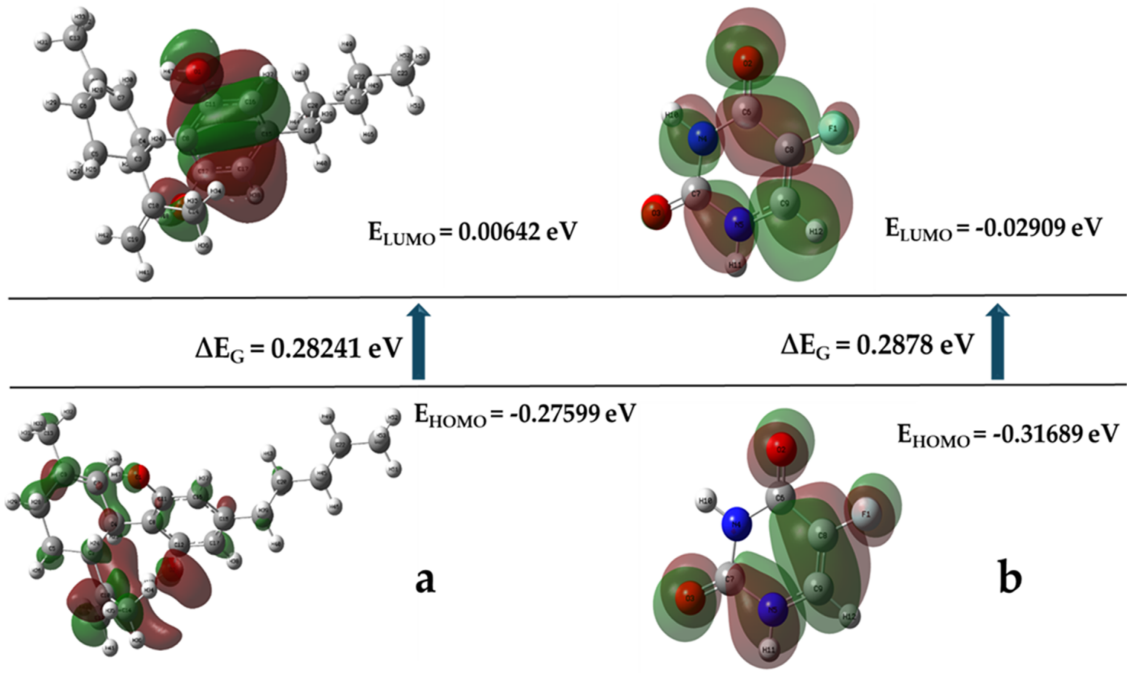

FIGURE 2 | The frontier molecular orbital of (a) cannabidiol and (b) 5-fluorouracil.

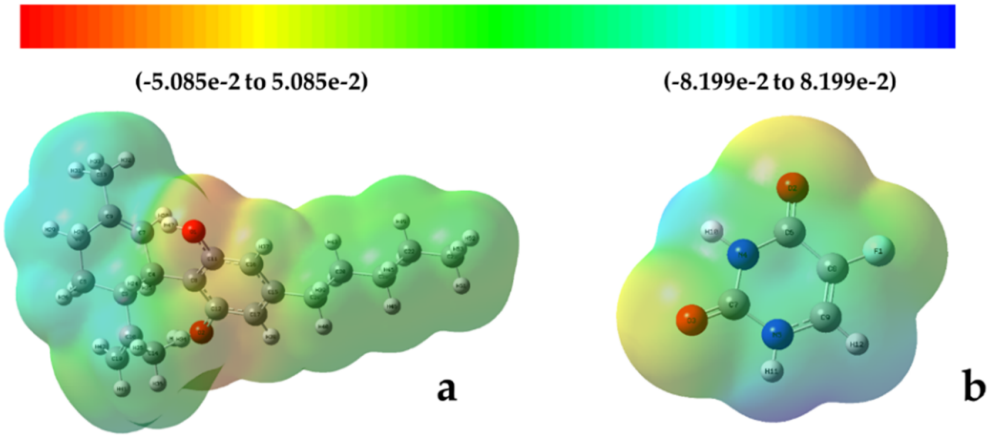

FIGURE 3 | Molecular electrostatic potential of (a) cannabidiol and (b) 5-fluorouracil.

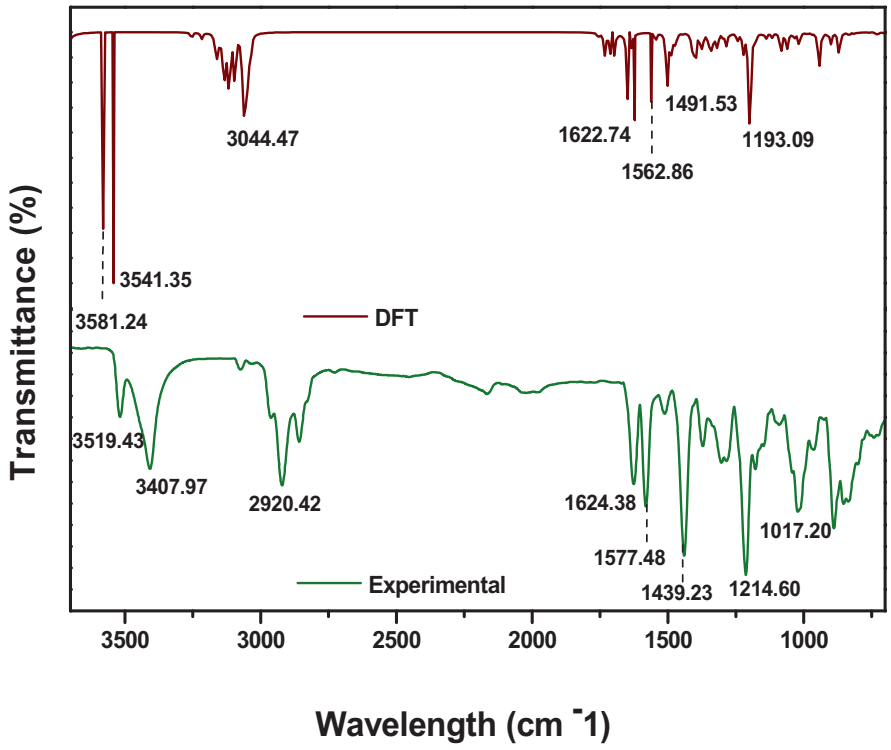

FIGURE 4 | Theoretically simulated and experimental FTIR of cannabidiol.

correlating to the theoretical value of 3581 cm^{-1} with a minimal difference of 62 cm^{-1}. The O–H stretch in alcohols/phenols exhibits a larger variance of 133 cm^{-1}, attributed to hydrogen bonding [78]. The C–H stretch/O–H dimer in alkanes/carboxylic acids differs by 124 cm^{-1}, possibly due to dimerization effects [79]. The Ar-CH=CHR stretch in alkenes demonstrates a strong correlation between experimental (1624 cm^{-1}) and theoretical (1622 cm^{-1}) values. In addition, minimal wavenumber variations are observed between experimental and theoretical values for the C–O stretch in carboxylic acids, Ar C–C stretch in aromatics, and C–H wag in alkyl halides, with differences of 14, 53, and 22 cm^{-1}, respectively. The DFT calculations correspond with experimental data, validating that the theoretical predictions exhibit computational accuracy. The close alignment of scaled theoretical frequencies with experimental values further validates the accuracy of the scaling factor used for vibrational frequency predictions (Table 3).

The VEDA Table S7 supports the findings by confirming the correlation between experimental FTIR wavenumbers and theoretical DFT calculations. Key observations include strong CH stretching vibrations at 3501.74 cm^{-1} (62%), 2190.07 cm^{-1} (60%), and 1938.12 cm^{-1} (57%), which demonstrate concordance with the experimental values for O–H and C–H stretches in alcohols and carboxylic acids. The initial analysis identified complex mixed modes at 2704.61 cm^{-1}, involving CH stretching, HCH bending, and HCCC torsion. The VEDA data reflect these mixed modes through variations in OH stretching, attributable to hydrogen bonding effects. Dominant HCCC torsion occurs at 2379.25 cm^{-1} (34%), while HCH bending is observed at

1982.81 cm^{-1} (32%) and HCC bending at 1341.53 cm^{-1} (22%). These bending vibrations align with the experimental and theoretical predictions.

3.6 | UV Analysis

UV–vis spectroscopy is an analytical technique that measures molecular absorption, revealing electronic transitions and providing insights into molecular structure [80]. The two aromatic rings in CBD facilitate $\pi-\pi^*$ transitions, where electrons delocalize across alternating double and single bonds, leading to absorption in the UV region, as observed at 281 and 274 nm in the experimental data (Figure 5 and Table 4). Additionally, the oxygen atoms in CBD, possess lone pairs and therefore participate in $n-\pi^*$ transitions. The minor wavelength variation between the two peaks may result from differing electronic environments of the aromatic rings or lone pair electrons on the oxygen atoms, leading to different transition energies [81]. The calculated UV–vis data identifies the first excited state at 241.53 nm with an oscillator strength of 0.0168, driven primarily by the 85 → 88 (2.54%) and 86 → 93 (21.66%) orbital transitions, resulting in a band gap of 5.1332 eV. The corresponding experimental peak is observed at 281 nm. The second excited state occurs at 223.56 nm with a decreased oscillator strength of 0.0004, dominated by the 86 → 87 (56.92%) transition, yielding a calculated band gap of 5.5459 eV. The related experimental peak is 274 nm. The difference in band gaps between theoretical and experimental is 0.7232 and 10 159 eV, respectively, suggesting a higher energy in the experimental observation. The third excited state is 218.34 nm with an oscillator strength of 0.0059, involving the 85 → 87 (24.18%) and 85 → 88 (40.56%) transitions, with a band gap of 5.6786 eV. Although no direct experimental peak corresponds to this state, the theoretical data are consistent with transitions observed in close proximity. Vibronic coupling in experimental spectra results in broadened peaks, obscuring distinct features [82]. In contrast, DFT predicts sharper transitions, therefore, peak broadening may not be observed [83].

TABLE 2 | Unscaled and scaled theoretical vibrational wavenumbers of cannabidiol with corresponding infrared intensities obtained from DFT analysis.

Experimental wave number	Calculated frequency (cm^{-1}) — M06-2X/6-31+G(d,p)		
	Unscaled	Scaled	IR
1578	1641	1563	72.31048
1624	1704	1623	64.99395
3408	3720	3541	−2.50E−07
3519	3762	3581	21.61261

3.7 | SWISS ADME Analysis

Swiss ADME (absorption, distribution, metabolism, and excretion) analysis was employed to assess and compare the physicochemical properties, pharmacokinetics, and drug-likeness of CBD with 5-FU (Table 5).

Within the drug discovery and development field, Lipinski's rule of five (RO5) is predominately employed as a pivotal guideline for identifying optimal drug molecules [84]. According to RO5, a drug compound with a molecular weight < 500 g/mol, hydrogen bond donors < 5, hydrogen bond acceptor sites < 10, and a $\log p < 5$, is said to have enhanced bioavailability properties associated with an organism's metabolic processes and increased pharmacokinetic characteristics [84, 85]. A recent study has expanded these criteria to include a polar surface area (PSA) of ≤ 140 $Å^2$ and fewer than 10 rotatable bonds [86]. A lower PSA indicates a molecule's ability to permeate cell membranes, with structures exceeding a PSA of 140 $Å^2$ demonstrating poor cellular permeability [87]. Table 5 highlights the PSA values for CBD and 5-FU, which are 40.46 and 65.72 $Å^2$, respectively. The lower PSA of CBD suggests increased cell membrane permeability compared to 5-FU.

The flexibility of a molecule is linked to the number of rotatable bonds, which is crucial for intracellular movement and effective binding interactions. A successful drug candidate should contain eight or fewer rotatable bonds to ensure adequate flexibility without excessive conformational freedom [88]. The CBD molecule exhibits six rotatable bonds, which present balanced flexibility that may enhance interaction with various biological targets, compared to 5-FU, which has no rotatable bonds. Additionally, CBD reflects a skin permeation value of −3.59 cm/s indicating a greater skin permeability, compared to 5-FU. According to the linear model of skin permeability formulated by Potts and Guy, which explains that a more negative log *K*p value results in a less skin permeant molecule [89]. Both CBD and 5-FU exhibit

TABLE 3 | Experimental and theoretical wavenumbers of cannabidiol with corresponding functional group assignments.

Experimental wavenumber (cm^{-1})	Theoretical wavenumber (cm^{-1})	Group bond	Functional group
3519	3581	O–H stretch	Alcohols
3408	3541	O–H stretch	Alcohols/phenols
2920	3044	C–H stretch/O–H dimer	Alkanes/carboxylic acids
1624	1623	Ar–CH=CHR	Alkenes
1577	1563	C–O stretch	Carboxylic acids
1439	1492	Ar C–C stretch	Aromatics
1215	1193	C–H wag	Alkyl halides

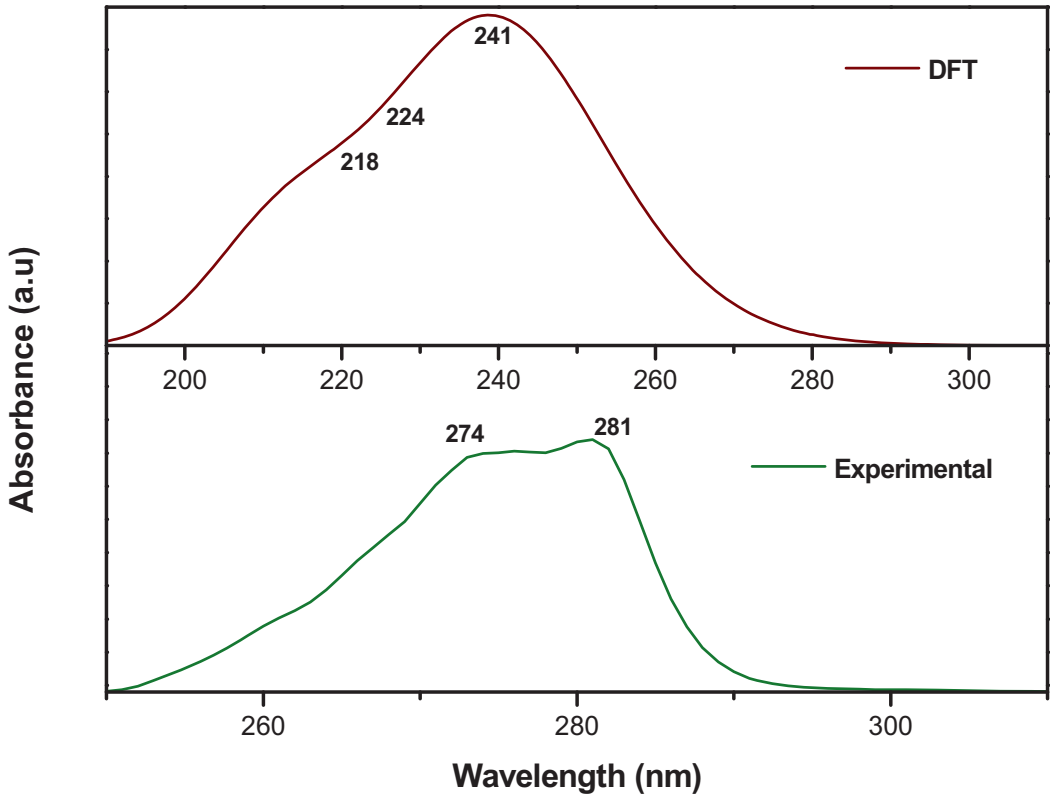

FIGURE 5 | Comparative theoretical and experimental UV–vis spectra of cannabidiol.

TABLE 4 | Theoretical and experimental UV–vis data of cannabidiol.

	Calculated					Experimental	
Excited state	Wavelength (nm)	Oscillator strength (f)	Key orbital contributions	Contribution (%)	Band gap (eV)	Wavelength (nm)	Band gap (eV)
1	241.53	0.0168	85 → 88	2.54	5.1332	281	4.41
			85 → 97	3.22			
			85 → 98	5.13			
			85 → 99	5.32			
			85 → 100	6.44			
			86 → 89	5.45			
			86 → 90	3.47			
			86 → 91	7.34			
			86 → 92	11.85			
			86 → 93	21.66			
			86 → 94	5.79			
			86 → 95	4.93			
			86 → 96	3.25			
			86 → 97	10.25			
2	223.56	0.0004	86 → 87	56.92	5.5459	274	4.53
			86 → 88	37.92			
			86 → 92	5.16			
3	218.34	0.0059	85 → 87	24.18	5.6786		
			85 → 88	40.56			

TABLE 5 | Comparative profile analysis of cannabidiol and 5-fluorouracil.

Properties	Cannabidiol	5-Fluorouracil
Physicochemical		
Formula	$C_{21}H_{30}O_2$	$C_4H_3FN_2O_2$
Molecular weight	314.46 g/mol	130.08 g/mol
Number of heavy atoms	23	9
Number of aromatic heavy atoms	6	6
Number of rotatable bonds	6	0
Fraction Csp3	0.52	0.0
Number of hydrogen (H) bond acceptors	2	3
Number of hydrogen (H) bond donors	2	2
Polar surface area (PSA)	40.46 Å^2	65.72 Å^2
Pharmacokinetics		
Skin permeation (log K_p)	−3.59 cm/s	−7.73 cm/s
Drug-likeness		
Bioavailability score	0.55	0.55
GI absorption	High	High
BBB permeant	Yes	No
Lipophilicity		
Consensus log P	5.20	0.13
Medicinal chemistry		
Pains	0 alert	0 alert

a bioavailability score of 0.55, suggesting a greater than 10% oral bioavailability in rat models [90].

The higher molecular weight of CBD (314.46 g/mol) implies a more complex structure that could engage in multiple interactions with biological targets, potentially enhancing specificity and efficacy [91]. Moreover, the fraction of sp^3 hybridized carbons in CBD (0.52) is associated with favorable pharmacokinetic properties and reduced promiscuity in drug-target interactions [92]. The absence of PAINS (Pan Assay Interference Compounds) alerts for CBD highlights its specificity and reliability as a drug candidate, minimizing the risk of nonspecific activity or assay artifacts including redox activity or metal chelation. This characteristic demonstrates that CBD's observed biological activity results from specific target interactions [93]. In the context of cSCC, CBD's specificity may reduce the potential for off-target effects.

3.8 | SWISS Target Prediction Analysis

Swiss target prediction analysis identifies potential molecular targets for the interaction with CBD. This method compares chemical fingerprints to classify molecules into families and identify molecules derived from the same chemical series [94]. Figure 6 illustrates the distribution of potential molecular targets that interact with CBD. The targets are categorized into different classes, with respective proportions. Family A G protein-coupled receptors are predicted to have the highest interaction probability with CBD. Table 6 lists three specific targets within the GPCR family, including CB1 and CB2, which belong to the rhodopsin family of GPCRs. These receptors are characterized by a heptahelical polypeptide structure with an intracellular carboxy-terminal and an extracellular amino-terminal containing sites for N-linked glycosylation. Ligand binding to CB1 and CB2 occurs within the plasma membrane, a common feature among rhodopsin family receptors [95]. The CB1 and CB2 receptors are established targets within the human ECS [96], involved in various pathophysiological processes such as hypertension, metabolic syndromes, cancer, pain, and inflammation [97]. Cannabidiol functions as a partial antagonist at CB1 receptors and as an inverse agonist at CB2 receptors [98]. Previous studies indicate that G-protein coupled receptor 55 (GPR 55) exhibits binding affinity for phytocannabinoids, despite limited structural similarity to CB1 and CB2 receptors [95]. Functionally, GPR 55 is involved in pathophysiological processes similar to CB1 and CB2, including roles in vascular functions, metabolic disorders, cancer, pain, and motor coordination [96]. Cannabidiol acts as an antagonist by inhibiting GPR 55 [98]. Therefore, previous studies confirm and support the prediction analysis performed on CBD in the current study.

3.9 | Molecular Docking Analysis

Molecular docking predicts ligand binding orientations within a receptor-binding site [99]. A study by Ramirez and Caballero highlighted two main types of docking used in medicinal chemistry: self-docking and cross-docking. Self-docking involves re-docking a ligand from an experimentally determined protein-ligand complex within the same crystal structure, serving as a reference ligand. Cross-docking involves docking a ligand across different protein binding sites [100]. In this study, the molecular docking analysis comprises both self and cross-docking. Five protein targets functioning as receptors were selected for molecular cross-docking, with CBD as the ligand. Table 7 lists these receptors and their respective functional roles in the human body that contribute to the formation and/or progression of cSCC. Reference ligand docking was also conducted, and the results were compared to the cross-docking outcomes to evaluate CBD's potential as an anticancer treatment for SCC. Glide XP offers a semiquantitative analysis that ranks selected ligands based on their binding affinity to protein receptors using scoring functions [107]. It systematically searches for the optimal conformational, positional, and orientational placement of a docked ligand, followed by energy optimization. A low Glide score is representative of increased ligand affinity [108].

The docking results of the CBD molecule with various protein receptors are presented in Table 8. The CBD molecule exhibits the highest binding affinity to the CB1 receptor (5TGZ), with a docking score of −9.986 kcal/mol, compared to a significantly lower score of −3.760 kcal/mol for 5-FU. Across all evaluated receptors, CBD consistently shows a stronger affinity for CB1 and CB2 than 5-FU. Additionally, an RMSD of 0.75 Å between the crystal and docked CBD ligand for CB1 indicates close alignment, suggesting

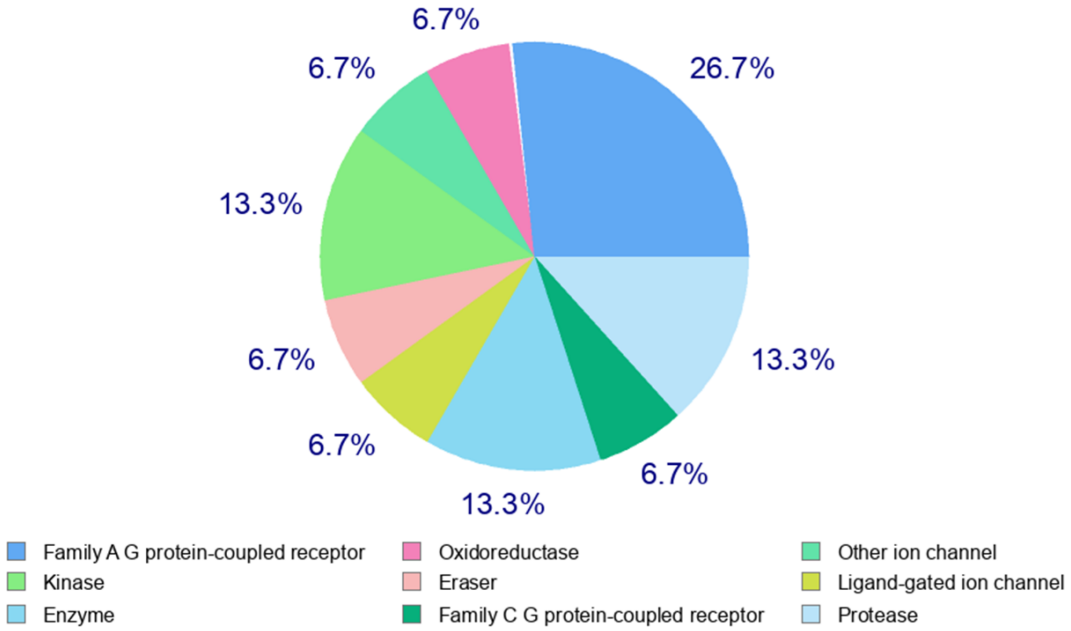

FIGURE 6 | Identification of potential molecular targets for cannabidiol interaction.

TABLE 6 | Molecular targets with the highest probability of cannabidiol interaction.

Target	Codes	ChEMBL ID	Target class
G-protein coupled receptor 55	GPR55	1 075 322	Family A G protein-coupled receptor
Cannabinoid receptor 1	CNR1	218	Family A G protein-coupled receptor
Cannabinoid receptor 2	CNR2	253	Family A G protein-coupled receptor

TABLE 7 | Five potential protein receptors for cannabidiol binding.

Receptor	PDB	Role	References
Cannabinoid receptor type 1 (Cb1)	5TGZ	Mediation of downstream signaling, immune function modulation	[101, 102]
Cannabinoid receptor type 2 (Cb2)	5ZTY	Immunomodulation target, postpone tumor progression	[103]
Epidermal growth factor	5ZTO	Skin cell proliferation, differentiation, tumorigenesis	[104]
Transforming protein p21 (GTPase HRas)	6DZH	Tumor induction and maintenance	[105]
Tumor protein p53	6GGA	Apoptosis, cell proliferation, DNA differentiation, and restoration	[106]

Abbreviation: PDB, Protein Data Bank.

that the docking accurately replicates the binding orientation of the crystal ligand (Figure 7). This structural congruence reinforces the reliability of CBD's favorable binding affinity and stable interaction with CB1.

Figure 8 displays the docking interaction between ligands (CBD and 5-FU) and the receptor (CB1). In the CBD binding pose (Figure 8a,b), the ligand engages in various hydrophobic and polar interactions with surrounding residues, PHE179, LEU193, TRP356, and CYS386. Cannabidiol anchors within the CB1 receptor's binding pocket by forming hydrogen bonds through its hydroxyl groups. Surrounding residues SER173, MET103, and GLY166 further stabilize the interaction via proximity and polar contacts, enhancing CBD's binding affinity. Conversely, the 5-FU binding pose (Figure 8c,d) exhibits reduced hydrophobic interactions, primarily interacting with residues PHE102, ILE169, and MET103. The binding interactions are stabilized through hydrogen bonds involving polar residues SER383, SER167, and GLY166. This suggests that 5-FU's interaction within the CB1 receptor relies more on polar interactions than the more extensive hydrophobic and polar network observed in CBD. The presence of fewer hydrophobic contacts and limited interaction with nonpolar residues may contribute to 5-FU's weaker binding affinity compared to CBD. The enhanced stability and increased interaction network of the CBD–CB1 complex correlates with CBD's higher binding affinity. A study by Casanova et al. [109], reported that activation of the CB1 receptor in SCC induces apoptosis, leading to tumor regression. The inhibition of angiogenesis further supports this antitumoral effect, as CB1 activation reduces the expression of VEGF, PIGF, and Ang2. These factors are critical for tumor-associated blood vessel development, a process essential for tumor growth

TABLE 8 | Self and cross-docking scores of cannabidiol in complex with receptor targets.

PDB code	Receptor name	Reference ligand code	Ref. lig score (kcal/mol)	Opt + freq. CBD	5-FU
5TGZ	CB1	ZDG	−12.686	−9.986	−3.760
		FMN	−12.741	−9.965	−5.959
5ZTO	Epidermal growth factor	9JO	−5.932	−2.880	−4.355
5ZTY	CB2	9JU	−12.186	−9.170	−3.864
6DZH	HRAS	GDP (Chain A)	−9.716	−4.843	−3.462
		GDP (Chain B)	−11.025	−3.099	−4.557
		GDP (Chain C)	−10.908	−4.843	−3.462
6GGA	P53	EY2 (Chain A)	−6.775	−5.146	−5.558
		EY2 (Chain B)	−6.776	−6.103	−3.864

Abbreviations: 5-FU, 5-fluorouracil; CBD, cannabidiol; PDB, Protein Data Bank.

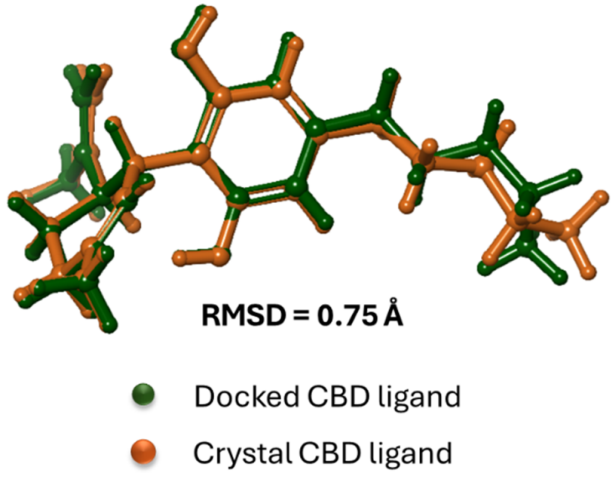

FIGURE 7 | Structural alignment of crystal and docked cannabidiol ligands.

and progression. Additionally, CB1 activation impairs epidermal growth factor receptor (EGFR) signaling, a key driver of angiogenesis and tumor expansion in SCC.

An unusual binding mechanism occurs when a ligand approaches the binding site of CB1 or CB2 receptors [110, 111], entering "sideways" through the lipid bilayer, as reported in previous MD studies [95]. Additionally, CB receptors feature a toggle switch that activates G-protein binding. The CB1 receptor contains a twin toggle switch involving two amino acid residues, F200 in transmembrane 3 (TM3) and W356 in TM6, while the CB2 receptor has a single toggle switch at residue W258 in TM6. This toggle switch mechanism causes the helices to open in a scissor form, allowing access to the G-protein binding site [112].

3.10 | Molecular Dynamics Simulation

The docked complexes of CBD–CB1 and 5-FU–CB1 (Figure 9) were further analyzed by a 250 ns MDS. Root mean square deviation (RMSD) quantifies structural differences by aligning the current structure of a ligand–protein complex to a reference for maximum overlap [113]. In this study, RMSD was employed to assess structural stability, model accuracy, and the equilibrium of the ligand within the protein binding site. In the CBD–CB1 complex, the CB1 receptor exhibits conformational flexibility in response to ligand binding. Furthermore, the RMSD of the CB1 increases to around 6 Å by 100 ns; thereafter, it stabilizes between 6 and 8 Å, indicating adaptive structural adjustments to accommodate CBD. The RMSD of CBD is maintained between 2 and 4 Å throughout the simulation, suggesting a consistent binding pose within the CB1 binding site. The observed stability is attributed to hydrogen bonding and hydrophobic interactions that firmly anchor CBD. This results in strong, specific interactions and a stable ligand–receptor complex characterized by receptor flexibility around a well-positioned ligand. In the 5-FU–CB1 complex, the CB1 receptor fluctuates between 2 and 6 Å from 0 to 145 ns, stabilizing around 4–5 Å for the remainder of the simulation. The RMSD of 5-FU ranges between 3 and 5 Å, indicating significant movement within the binding pocket and a less stable binding pose due to weaker or less specific interactions with CB1. This increased flexibility of 5-FU correlates with the receptor's higher conformational variability, reflecting a more transient and flexible binding mode.

The 2D interaction diagrams (Figure 10) from the MDS confirm the initial docking results by demonstrating the stability and persistence of key interactions between CBD and CB1 over 250 ns. Consistent hydrophobic and polar interaction frequencies for residues SER383 (45%) and PHE268 (38%) correlate with docking data, indicating that the docking-derived binding pose remains stable under dynamic conditions. In the case of 5-FU, three key residues ASP163, SER203, and PHE200 anchor it within the CB1 binding site. The ASP163 residue forms hydrogen bonds with 5-FU at a high interaction frequency of 74%, SER203 at 49%, and PHE200 contributes hydrophobic interactions at 34%. This limited interaction network accounts for 5-FU's higher RMSD fluctuations and weaker binding stability observed in both docking and MDS.

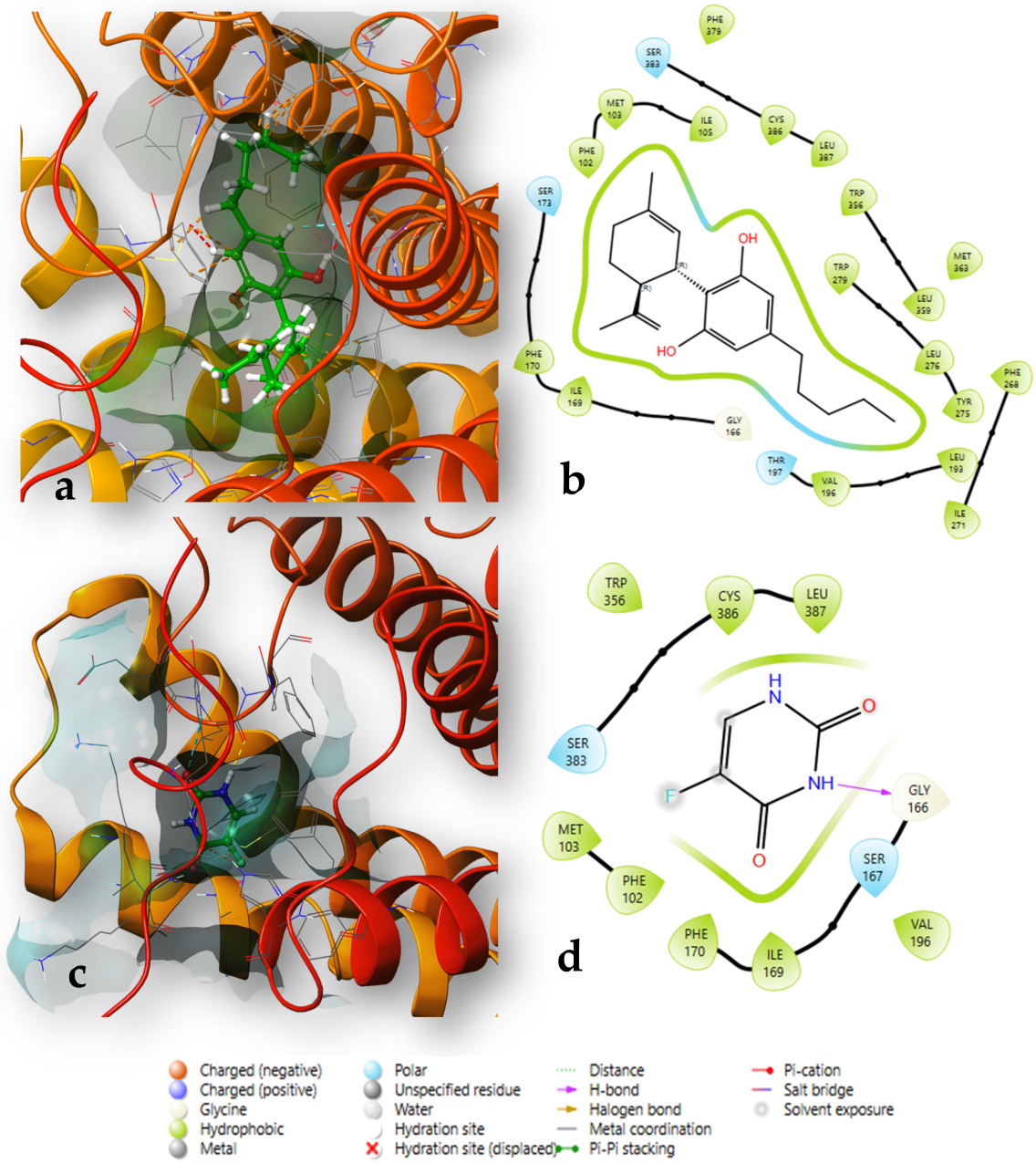

FIGURE 8 | Optimal binding poses and comparative docking interactions of cannabidiol (a and b) with 5-fluorouracil (c and d) within the CB1 receptor binding site (5TGZ).

3.11 | Binding Free Energy (MMGBSA) Analysis

The binding energies for CBD and 5-FU are presented in Table 9 and illustrated in Figure 11. The binding free energy (ΔG_{bind}) indicates that CBD (−69.6962 kcal/mol) exhibits a significantly stronger binding affinity than 5-FU (−28.2407 kcal/mol). The stronger affinity of CBD is attributed primarily to contributions from lipophilic (−32.0722 kcal/mol) and van der Waals (vdW; −47.8709 kcal/mol) interactions. These interactions stabilize the CBD binding within the CB1 receptor's hydrophobic pocket. In contrast, the weak contributions from lipophilic (−3.3419 kcal/mol) and vdW (−22.4239 kcal/mol) interactions suggest that 5-FU's binding is less stable within the hydrophobic core of the CB1 receptor. However, 5-FU demonstrates stronger electrostatic (Coulomb; −15.1755 kcal/mol) and hydrogen bonding (Hbond; −1.16326 kcal/mol). The reliance on polar interactions may limit 5-FU's ability to sustain receptor engagement in dynamic environments, potentially reducing its efficacy. Both CBD and 5-FU exhibit relatively small covalent and packing interaction contributions, while CBD incurs a higher solvation penalty ($\Delta G_{\text{bind solv GB}}$; 21.1375 kcal/mol) compared to 5-FU (14.5787 kcal/mol). These findings highlight the differences in binding mechanisms of CBD and 5-FU, with CBD characterized by hydrophobic and vdW-driven interactions, whereas 5-FU relies more on electrostatic and hydrogen bonding interactions.

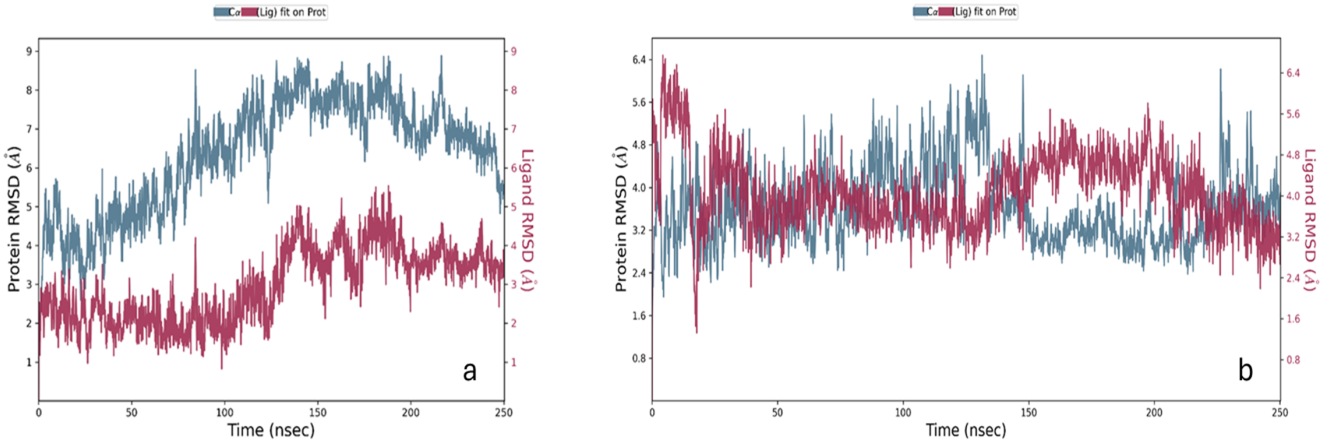

FIGURE 9 | Comparative root mean square deviation of (a) cannabidiol and (b) 5-fluorouracil in complex with cannabinoid receptor 1, over a 250 ns molecular dynamics simulation.

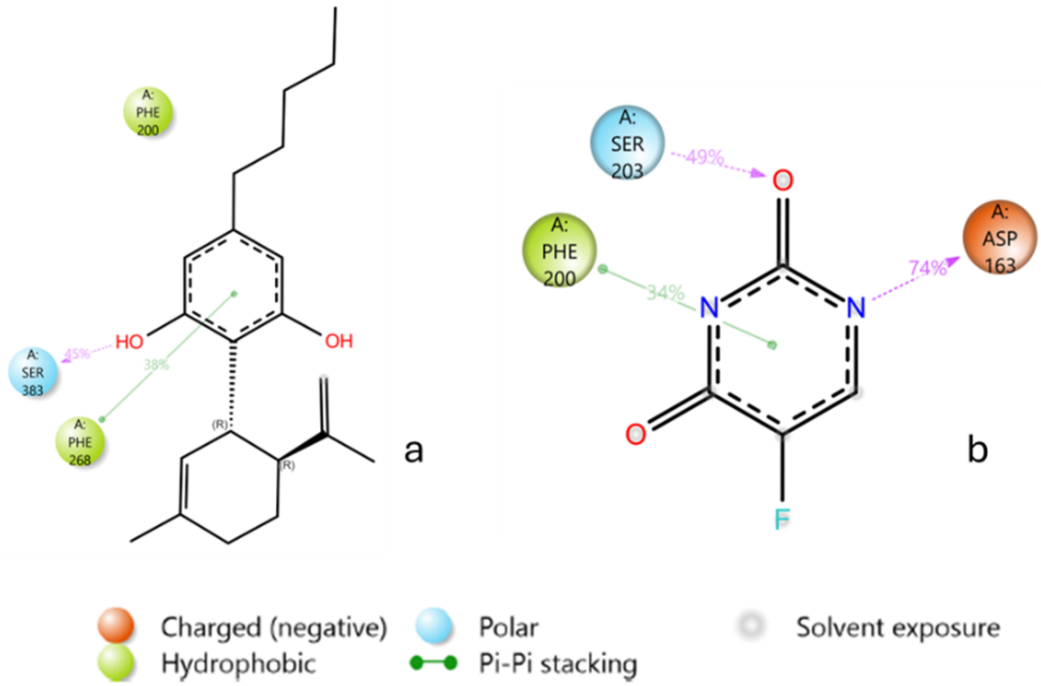

FIGURE 10 | Comparative interaction diagram of (a) cannabidiol and (b) 5-fluorouracil in complex with cannabinoid receptor 1.

3.12 | Cytotoxic Analyses

A cytotoxic evaluation of CBD was conducted against A431 cells to investigate its potential as an anticancer agent, using 5-FU as a positive control due to the established efficacy in cancer treatment. The SRB assay determined the half maximum inhibitory concentration (IC_{50}) values (Table 10 and Figure 12). Cannabidiol demonstrated a higher cytotoxicity compared to 5-FU, with IC_{50} values of 2.76 and 5.61 μM, respectively. In addition, CBD exhibited biological activity against SCC cells at low concentrations, as the cell density reduced by 39% when treated with the lowest CBD concentration (2.2 μM). In contrast, 5-FU exhibited minimal effect on A431 cells at 2.2 μM.

In comparison to other cell lines (Table 11), CBD presents with a higher cytotoxicity in the A431 cell line used in the current study,

TABLE 9 | Comparative binding energy parameters of cannabidiol and 5-fluorouracil.

Energy parameters	Cannabidiol (kcal/mol)	5-Fluorouracil (kcal/mol)
ΔG_{bind}	−69.6962	−28.2407
$\Delta G_{\_Coulomb}$	−10.6231	−15.1755
$\Delta G_{\_covalent}$	1.8572	0.1984
$\Delta G_{\_Hbond}$	−0.4917	−1.1633
$\Delta G_{\_lipo}$	−32.0722	−3.3419
$\Delta G_{\_packing}$	−1.633	−0.9132
$\Delta G_{\_solv\ GB}$	21.1375	14.5787
$\Delta G_{\_vdW}$	−47.8709	−22.4239

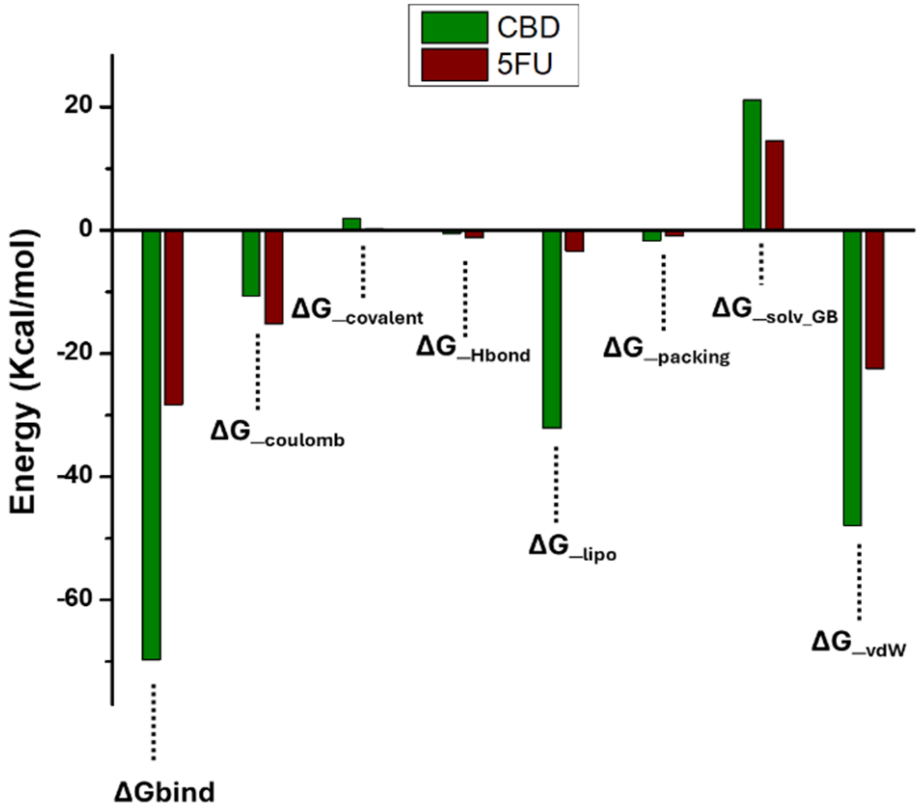

FIGURE 11 | Binding energy contributions for cannabidiol (green) and 5-fluorouracil (brown).

TABLE 10 | The IC_{50} values of cannabidiol and 5-fluorouracil against squamous cell carcinoma (A431).

Drug compound	$IC_{50} \pm SEM$ (μM) on A431 cell lines
CBD	2.76 ± 1.08
5-FU (positive control)	5.61 ± 1.07

Abbreviations: 5-FU, 5-fluorouracil; A431, squamous carcinoma cells; CBD, cannabidiol; IC_{50}, half-maximal inhibitory concentration; SEM, standard mean error.

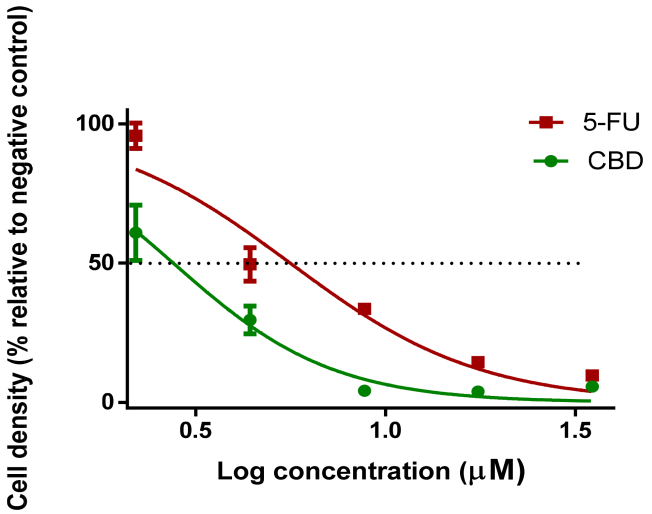

FIGURE 12 | The cytotoxic effect of cannabidiol and 5-fluorouracil on squamous cell carcinoma. The black dashed line represents a 50% cell density.

with only cervical cancer cells (SiHa and HeLa) showing similar sensitivity (IC_{50} of 3.20 μM). However, several factors may contribute to such effects, including the different cytotoxicity assays, cell lines, and time of exposure to CBD. Previous studies indicate that CB1 and CB2 receptors are overexpressed in several tumor cells, including SCC [118], relative to nontumor cells [119]. The molecular docking analyses in this study demonstrate that CBD exhibits the highest binding affinity toward the CB1 receptor. An overexpression of the CB1 receptor facilitates an increased CBD binding rate, which may contribute to its increased cytotoxicity compared to 5-FU. The CB1 receptor-CBD complex induces cell death through several mechanisms. The CBD activates caspase-8, caspase-9, and caspase-3, leading to apoptosis and increased ROS generation, promoting mitochondrial dysfunction [120]. Upon activation, the CB1 receptor, coupled with Gi/o proteins, inhibits adenylate cyclase, reducing cAMP levels and PKA activity. This downregulates gene transcription involved in cell survival, contributing to the antiproliferative and proapoptotic effects of CBD [121].

4 | Conclusion

This study provides a mechanistic understanding of the enhanced cytotoxicity of CBD relative to 5-FU against A431 cells, by integrating quantum chemical analysis, molecular docking, and MDS. Quantum data reveal CBD's stable electron distribution and increased reactivity due to a small HOMO–LUMO gap. Cannabidiol's heightened reactivity facilitates stable interactions with the CB1 receptor and supports its flexibility and adaptability in biological interactions. Molecular docking

TABLE 11 | Cytotoxicity of cannabidiol in various cancer cell lines.

Cancer cell line	Screening method	IC_{50} (μM)	Exposure time frame (h)	References
Human breast (MDA-MB-231)	Crystal violet assay	10.60	96	[114]
Human breast (MCF-7)	Crystal violet assay	8.20	96	[114]
Rat glioma (C_6)	Crystal violet assay	8.50	96	[114]
Human colorectal (CaCo-2)	Crystal violet assay	7.50	96	[114]
Human cervical (SiHa)	MTT assay	3.20	22	[115]
Human cervical (HeLa)	MTT assay	3.20	22	[115]
Human prostate (DU145)	MTT assay	5.40	72	[116]
Lung (A549)	MTT assay	36.70	36	[117]
Melanoma (B16)	MTT assay	38.69	36	[117]

Abbreviations: IC_{50}, IC_{50} indicates half-maximal inhibitory concentration; MIT, MTT assay is a colorimetric assay used to measure cytotoxicity in cancer cells via the conversion of MTT (3-(4,5-dimethylthiazol-2-yl)-2,5-diphenyltetrazolium bromide) to purple formazan.

results further demonstrate CBD's increased affinity to the CB1 receptor, with a docking score of −9.986 kcal/mol, exceeding 5-FU (−3.760 kcal/mol). In contrast, 5-FU's rigid, planar conformation dominated by electron-withdrawing groups limits its adaptability and reduces receptor-binding efficacy. The enhanced binding between CBD and the CB1 receptor is due to conformational versatility and favorable bond geometries that enable robust and sustained ligand-receptor interactions. The MDS and MMGBSA analyses corroborate these findings, indicating CBD's strong and stable binding to the CB1 receptor, primarily driven by hydrophobic and van der Waals interactions. Conversely, 5-FU's interaction profile is comparatively weaker and relies more on transient polar interactions.

The Fukui and ESP analyses further validate the findings, CBD's balanced reactivity and moderate ESP with evenly distributed nucleophilic and electrophilic regions, supporting stable and versatile interactions. In contrast, 5-FU's localized reactivity and polarized ESP align with its reliance on specific polar interactions, limiting its binding stability.

Additionally, the experimental FTIR and UV–vis analyses serve to validate the computational calculations. The strong correlation between the experimental and theoretical FTIR spectra confirms the accuracy of the selected functional and basis set, reinforcing the reliability of the computational methodology. Although the UV–vis results exhibit some deviations, likely attributable to limitations in the TDDFT level of theory, they remain broadly consistent with the computationally predicted electronic transitions, further supporting the theoretical framework.

The increased stability observed in CBD–CB1 binding highlights potential mechanisms underlying cell death. This includes apoptosis induction, caspase activation, ROS generation, and the inhibition of adenylate cyclase, leading to reduced cAMP levels and downregulated gene transcription. The cytotoxicity assays reveal that CBD exhibited a lower IC_{50} value (2.76 ± 1.08 μM) compared to 5-FU (5.61 ± 1.07 μM) in A431 SCC cells. This suggests the enhanced efficacy of CBD in reducing cell density at lower concentrations, further supported by its capacity to reduce cell density by 39% at the lowest dose tested.

These findings provide a robust foundation for the further development of CBD as a therapeutic agent for cSCC, with the potential to enhance current treatment paradigms.

Future studies should include comparative binding studies with other cannabinoids that could further clarify CBD's specificity for the CB1 receptor. Machine learning models could be used to predict the activity, toxicity, and ADMET properties of novel CBD derivatives. Given the promising in vitro results, future research should also prioritize in vivo validation of CBD's anticancer effects and investigations into potential combination therapies.

Author Contributions

Software: Krishna Kuben Govender and Andrea Jess Josiah. Data curation and analysis: Andrea Jess Josiah, Krishna Kuben Govender, and Werner Cordier. Conceptualization and writing: Andrea Jess Josiah and Krishna Kuben Govender. Cytotoxicity analysis technical support: Margo Nell. Review and editing: Krishna Kuben Govender, Penny Poomani Govender, and Suprakas Sinha Ray.

Acknowledgments

A.J.J. and S.S.R. thank the Department of Science and Innovation and the Council for Scientific and Industrial Research for financial support. A.J.J., K.K.G., and P.P.G. acknowledge the Centre for High Performance Computing (CHPC) in Cape Town, South Africa, for providing access to the computational resources utilized in this study.

Funding

The authors have nothing to report.

Conflicts of Interest

The authors declare no conflicts of interest.

Data Availability Statement

The data that support the findings of this study are available from the corresponding author upon reasonable request.

References

1. The Global Challenge of Cancer," *Nature Cancer* 1 (2020): 1–2, https://doi.org/10.1038/s43018-019-0023-9.

2. J. Ferlay, M. Ervik, F. Lam, M. Colombet, L. Mery, and M. Piñeros, *Global Cancer Observatory: Cancer Today* (International Agency for Research on Cancer, 2020).

3. L. Lugasi, I. Grinberg, and S. Margel, "Targeted Delivery of CBD-Loaded Poly (RGD) Proteinoid Nanoparticles for Antitumor Therapy," *Journal of Nanomedicine & Nanotechnology* 11, no. 6 (2020): 1–12, https://doi.org/10.35248/2157-7439.20.11.552.

4. Skin Cancer Foundation, *Skin Cancer Information*, accessed February 18, 2024, https://www.skincancer.org/skin-cancer-information/.

5. C. Garbe and U. Leiter, "Epidemiology of Melanoma and Nonmelanoma Skin Cancer—The Role of Sunlight," in *Advances in Experimental Medicine and Biology*, vol. 624 (Springer New York, 2008), 89–103, https://doi.org/10.1007/978-0-387-77574-6_8.

6. C. Karimkhani, L. N. Boyers, R. P. Dellavalle, and M. A. Weinstock, "It's Time for "Keratinocyte Carcinoma" to Replace the Term "Nonmelanoma Skin Cancer"," *Journal of the American Academy of Dermatology* 72, no. 1 (2015): 186–187.

7. D. Didona, G. Paolino, U. Bottoni, and C. Cantisani, "Non Melanoma Skin Cancer Pathogenesis Overview," *Biomedicine* 6, no. 1 (2018): 6.

8. Skin Cancer Foundation, *Skin Cancer Facts & Statistics*, accessed November 3, 2023, https://www.skincancer.org/skin-cancer-information/skin-cancer-facts/.

9. P. S. Karia, J. Han, and C. D. Schmults, "Cutaneous Squamous Cell Carcinoma: Estimated Incidence of Disease, Nodal Metastasis, and Deaths From Disease in the United States, 2012," *Journal of the American Academy of Dermatology* 68, no. 6 (2013): 957–966, https://doi.org/10.1016/j.jaad.2014.09.036.

10. E.-C. Cozma, L. M. Banciu, C. Soare, and S.-M. Cretoiu, "Update on the Molecular Pathology of Cutaneous Squamous Cell Carcinoma," *International Journal of Molecular Sciences* 24, no. 7 (2023): 6646, https://doi.org/10.3390/ijms24076646.

11. R. Jiang, M. Fritz, and S. K. T. Que, "Cutaneous Squamous Cell Carcinoma: An Updated Review," *Cancers* 16, no. 10 (2024): 1800, https://doi.org/10.3390/cancers16101800.

12. N. G. Amôr, P. S. d. S. Santos, and A. P. Campanelli, "The Tumor Microenvironment in SCC: Mechanisms and Therapeutic Opportunities," *Frontiers in Cell and Developmental Biology* 9 (2021): 636544, https://doi.org/10.3389/fcell.2021.636544.

13. B. Azzimonti, E. Zavattaro, M. Provasi, et al., "Intense Foxp3+ CD25+ Regulatory T-Cell Infiltration Is Associated With High-Grade Cutaneous Squamous Cell Carcinoma and Counterbalanced by CD8+/Foxp3+ CD25+ Ratio," *British Journal of Dermatology* 172, no. 1 (2015): 64–73, https://doi.org/10.1111/bjd.13172.

14. D. Saadeh, M. Kurban, and O. Abbas, "Plasmacytoid Dendritic Cell Role in Cutaneous Malignancies," *Journal of Dermatological Science* 83, no. 1 (2016): 3–9, https://doi.org/10.1016/j.jdermsci.2016.05.008.

15. P. Cammareri, A. M. Rose, D. F. Vincent, et al., "Inactivation of TGFβ Receptors in Stem Cells Drives Cutaneous Squamous Cell Carcinoma," *Nature Communications* 7 (2016): 12493, https://doi.org/10.1038/ncomms12493.

16. C. R. Pickering, J. H. Zhou, J. J. Lee, et al., "Mutational Landscape of Aggressive Cutaneous Squamous Cell Carcinoma," *Clinical Cancer Research* 20, no. 24 (2014): 6582–6592, https://doi.org/10.1158/1078-0432.ccr-14-1768.

17. V. L. Brown, C. A. Harwood, T. Crook, J. G. Cronin, D. P. Kelsell, and C. M. Proby, "P16INK4a and p14ARF Tumor Suppressor Genes Are Commonly Inactivated in Cutaneous Squamous Cell Carcinoma," *Journal of Investigative Dermatology* 122, no. 5 (2004): 1284–1292, https://doi.org/10.1111/j.0022-202x.2004.22501.x.

18. A. P. South, K. J. Purdie, S. A. Watt, et al., "NOTCH1 Mutations Occur Early During Cutaneous Squamous Cell Carcinogenesis," *Journal of Investigative Dermatology* 134, no. 10 (2014): 2630–2638, https://doi.org/10.1038/jid.2014.154.

19. M. A. Nelson, J. G. Einspahr, D. S. Alberts, et al., "Analysis of the P53 Gene in Human Precancerous Actinic Keratosis Lesions and Squamous Cell Cancers," *Cancer Letters* 85, no. 1 (1994): 23–29, https://doi.org/10.1016/0304-3835(94)90234-8.

20. I. Pastushenko, F. Mauri, Y. Song, et al., "Fat1 Deletion Promotes Hybrid EMT State, Tumour Stemness and Metastasis," *Nature* 589, no. 7842 (2021): 448–455, https://doi.org/10.1038/s41586-020-03046-1.

21. G. T. Prince, M. C. Cameron, R. Fathi, and T. Alkousakis, "Topical 5-Fluorouracil in Dermatologic Disease," *International Journal of Dermatology* 57, no. 10 (2018): 1259–1264, https://doi.org/10.1111/ijd.14106.

22. B. C. Rudy and B. Z. Senkowski, "Fluorouracil," *Analytical Profiles of Drug Substances and Excipients* 2 (1973): 221–244, https://doi.org/10.1016/S0099-5428(08)60041-6.

23. J. Casale and P. Patel, "Fluorouracil," in *StatPearls* (StatPearls Publishing, 2024), accessed November 7, 2023, https://www.ncbi.nlm.nih.gov/books/NBK549808/.

24. E. H. Yoo and J. H. Lee, "Cannabinoids and Their Receptors in Skin Diseases," *International Journal of Molecular Sciences* 24, no. 22 (2023): 16523, https://doi.org/10.3390/ijms242216523.

25. D. Abrams and M. Guzman, "Cannabis in Cancer Care," *Clinical Pharmacology and Therapeutics* 97 (2015): 575–586, https://doi.org/10.1002/cpt.108.

26. World Health Organization, "Technical Report Series 1013 1, Cannabidiol (CBD)," in *Critical Review Report. Expert Committee on Drug Dependence. Fortieth Meeting* (2018), accessed December 15, 2023.

27. K. F. Tóth, D. Ádám, T. Bíró, and A. Oláh, "Cannabinoid Signaling in the Skin: Therapeutic Potential of the "C(Ut)Annabinoid" System," *Molecules* 24, no. 5 (2019): 918, https://doi.org/10.3390/molecules24050918.

28. R. Ramer, F. Wendt, F. Wittig, et al., "Impact of Cannabinoid Compounds on Skin Cancer," *Cancers* 14, no. 7 (2022): 1769, https://doi.org/10.3390/cancers14071769.

29. M. Nikan, S. M. Nabavi, and A. Manayi, "Ligands for Cannabinoid Receptors, Promising Anticancer Agents," *Life Sciences* 146 (2016): 124–130, https://doi.org/10.1016/j.lfs.2015.12.053.

30. S. M. Baswan, A. E. Klosner, K. Glynn, et al., "Therapeutic Potential of Cannabidiol (CBD) for Skin Health and Disorders," *Clinical, Cosmetic and Investigational Dermatology* 13 (2020): 927–942, https://doi.org/10.2147/ccid.s286411.

31. S. M. Amini and A. Akbari, "Metal Nanoparticles Synthesis Through Natural Phenolic Acids," *IET Nanobiotechnology* 13 (2019): 771–777, https://doi.org/10.1049/iet-nbt.2018.5386.

32. M. Kassim, M. Achoui, M. R. Mustafa, M. A. Mohd, and K. M. Yusoff, "Ellagic Acid, Phenolic Acids, and Flavonoids in Malaysian Honey Extracts Demonstrate In Vitro Anti-Inflammatory Activity," *Nutrition Research* 30 (2010): 650–659, https://doi.org/10.1016/j.nutres.2010.08.008.

33. P. Gohad, J. McCoy, C. Wambier, et al., "Novel Cannabidiol Sunscreen Protects Keratinocytes and Melanocytes Against Ultraviolet B Radiation," *Journal of Cosmetic Dermatology* 20, no. 4 (2021): 1350–1352, https://doi.org/10.1111/jocd.13693.

34. Y. Maor, J. Yu, P. M. Kuzontkoski, B. J. Dezube, X. Zhang, and J. E. Groopman, "Cannabidiol Inhibits Growth and Induces Programmed Cell Death in Kaposi Sarcoma-Associated Herpesvirus-Infected Endothelium," *Genes & Cancer* 3, no. 7–8 (2012): 512–520, https://doi.org/10.1177/1947601912466556.

35. M. D. Mashabela and A. P. Kappo, "Anti-Cancer and Anti-Proliferative Potential of Cannabidiol: A Cellular and Molecular Perspective," *International Journal of Molecular Sciences* 25, no. 11 (2024): 5659, https://doi.org/10.3390/ijms25115659.

36. Y. Y. Go, S. R. Kim, D. Y. Kim, S.-W. Chae, and J.-J. Song, "Cannabidiol Enhances Cytotoxicity of Anti-Cancer Drugs in Human Head and Neck Squamous Cell Carcinoma," *Scientific Reports* 10, no. 1 (2020): 20622, https://doi.org/10.1038/s41598-020-77674-y.

37. A. Cavalli, P. Carloni, and M. Recanatini, "Target-Related Applications of First Principles Quantum Chemical Methods in Drug Design," *Chemical Reviews* 106 (2006): 3497–3519, https://doi.org/10.1021/cr050579p.

38. J. C. A. Boeyens, "Molecular Structure," in *New Theories for Chemistry* (Elsevier, 2005), 177–227, https://doi.org/10.1016/B978-044451867-5/50006-3.

39. F. Jensen, *Introduction to Computational Chemistry*, 3rd ed. (John Wiley & Sons, 2017), 1–3.

40. A. J. Josiah, K. K. Govender, P. P. Govender, and S. Sinha Ray, "Advancements and Perspectives in Folate-Based Anticancer Drugs: Bridging Quantum and Classical Mechanics in Folate Receptor Research," *Advanced Theory and Simulations* 7, no. 8 (2024): 2400377, https://doi.org/10.1002/adts.202400377.

41. I. Ahmad, V. Jagatap, and H. Patel, "Application of Density Functional Theory (DFT) and Response Surface Methodology (RSM) in Drug Discovery," in *Phytochemistry, Computational Tools and Databases in Drug Discovery* (Elsevier, 2023), 371–392, https://doi.org/10.1016/B978-0-323-90593-0.00004-6.

42. T. van Mourik, M. Bühl, and M.-P. Gaigeot, "Density Functional Theory Across Chemistry, Physics and Biology," *Philosophical Transactions of the Royal Society A: Mathematical, Physical and Engineering Sciences* 372 (2014): 20120488, https://doi.org/10.1098/rsta.2012.0488.

43. O. C. Adekoya, G. J. Adekoya, E. R. Sadiku, Y. Hamam, and S. S. Ray, "Application of DFT Calculations in Designing Polymer-Based Drug Delivery Systems: An Overview," *Pharmaceutics* 14 (2022): 1972, https://doi.org/10.3390/pharmaceutics14091972.

44. Y. Zhao and D. G. Truhlar, "The M06 Suite of Density Functionals for Main Group Thermochemistry, Thermochemical Kinetics, Noncovalent Interactions, Excited States, and Transition Elements: Two New Functionals and Systematic Testing of Four M06-Class Functionals and 12 Other Functionals," *Theoretical Chemistry Accounts* 120 (2008): 215–241, https://doi.org/10.1007/S00214-007-0310-X/METRICS.

45. P. F. Provasi, L. Modesto-Costa, F. Sampaio, et al., "The Importance of the Density Functional Theory Exchange-Correlation Hartree-Fock Term in Magnetic Resonance: Application to an Aqueous Environment," *Journal of Physical Chemistry. A* 127 (2023): 619–626.

46. *11.4: Orbital Polarization Terms in Basis Sets* (2020), accessed May 3, 2024, https://chem.libretexts.org/Courses/Pacific_Union_College/Quantum_Chemistry/11%3A_Computational_Quantum_Chemistry/11.04%3A_Orbital_Polarization_Terms_in_Basis_Sets.

47. D. C. Sherrill, *Basis Sets in Quantum Chemistry* (Gatech.edu), accessed April 18, 2024, http://vergil.chemistry.gatech.edu/courses/chem6485/pdf/basis-sets.pdf.

48. K. E. Riley, B. T. Op't Holt, and K. M. Merz, "Critical Assessment of the Performance of Density Functional Methods for Several Atomic and Molecular Properties," *Journal of Chemical Theory and Computation* 3 (2007): 407–433, https://doi.org/10.1021/ct600185a.

49. Gaussian 16, Revision B.01, M. J. Frisch, G. W. Trucks, et al., *GaussView 5.0* (Gaussian, Inc., 2016).

50. R. Dennington, T. A. Keith, and J. M. Millam, *GaussView 6.0.16* (Semichem Inc, 2016), Shawnee Mission. References Scientific Research Publishing, accessed June 20, 2023, https://www.scirp.org/reference/referencespapers?referenceid=3413212.

51. A. Pathak, A. Sayed Manik, K. Zahra Mehjabin, et al., "Molecular Docking and ADME/T Analysis for Identification of Novel Potential COX Inhibitors of Some Isolated Compounds From *Clausena lansium* for Analgesic Treatment," *Pharmaceutica Analytica Acta* 6, no. 9 (2018): 153–156.

52. A. Daina, O. Michielin, and V. Zoete, "SwissADME: A Free Web Tool to Evaluate Pharmacokinetics, Drug-Likeness and Medicinal Chemistry Friendliness of Small Molecules," *Scientific Reports* 7, no. 1 (2017): 1–13, https://doi.org/10.1038/srep42717.

53. M. H. Jamróz, "Vibrational Energy Distribution Analysis (VEDA): Scopes and Limitations," *Spectrochimica Acta. Part A, Molecular and Biomolecular Spectroscopy* 114 (2013): 220–230, https://doi.org/10.1016/j.saa.2013.05.096.

54. T. Lu and F. Chen, "Multiwfn: A Multifunctional Wavefunction Analyzer," *Journal of Computational Chemistry* 33 (2012): 580–592, https://doi.org/10.1002/jcc.22885.

55. Chpc:Lengau, *wiki.Chpc.Ac.Za* (Chpc.ac.za), accessed January 30, 2024, https://wiki.chpc.ac.za/chpc:lengau.

56. *RCSB PDB: Homepage*, accessed January 23, 2024, https://www.rcsb.org/.

57. *PubChem*, accessed January 23, 2024, https://pubchem.ncbi.nlm.nih.gov/.

58. H. B. Schlegel, "Optimization of Equilibrium Geometries and Transition Structures," *Journal of Computational Chemistry* 3 (1982): 214–218, https://doi.org/10.1002/jcc.540030212.

59. J. W. Ochterski, *Vibrational Analysis in Gaussian* (Gaussian.com), https://gaussian.com/wp-content/uploads/dl/vib.pdf1999.

60. *Creating UV/Visible Plots From the Results of Excited States Calculations* (Gaussian.com), accessed May 29, 2024, https://gaussian.com/uvvisplot/.

61. G. Madhavi Sastry, M. Adzhigirey, T. Day, R. Annabhimoju, and W. Sherman, "Protein and Ligand Preparation: Parameters, Protocols, and Influence on Virtual Screening Enrichments," *Journal of Computer-Aided Molecular Design* 27 (2013): 221–234, https://doi.org/10.1007/s10822-013-9644-8.

62. M. H. M. Olsson, C. R. Søndergaard, M. Rostkowski, and J. H. Jensen, "PROPKA3: Consistent Treatment of Internal and Surface Residues in Empirical p K_a Predictions," *Journal of Chemical Theory and Computation* 7 (2011): 525–537, https://doi.org/10.1021/ct100578z.

63. *Schrödinger Release 2024-3: Force Fields* (Schrödinger, LLC, 2024).

64. *Schrödinger Release 2024-3: Glide* (Schrödinger, LLC, 2024).

65. R. A. Friesner, J. L. Banks, R. B. Murphy, et al., "Glide: A New Approach for Rapid, Accurate Docking and Scoring. 1. Method and Assessment of Docking Accuracy," *Journal of Medicinal Chemistry* 47 (2004): 1739–1749, https://doi.org/10.1021/jm0306430.

66. C. Lu, C. Wu, D. Ghoreishi, et al., "OPLS4: Improving Force Field Accuracy on Challenging Regimes of Chemical Space," *Journal of Chemical Theory and Computation* 17 (2021): 4291–4300, https://doi.org/10.1021/acs.jctc.1c00302.

67. S. Genheden and U. Ryde, "The MM/PBSA and MM/GBSA Methods to Estimate Ligand-Binding Affinities," *Expert Opinion on Drug Discovery* 10, no. 5 (2015): 449–461, https://doi.org/10.1517/17460441.2015.1032936.

68. R. S. M. Rashid, S. Temurlu, A. Abourajab, et al., "Drug Repurposing of FDA Compounds Against α-Glucosidase for the Treatment of Type 2 Diabetes: Insights From Molecular Docking and Molecular Dynamics Simulations," *Pharmaceuticals* 16, no. 4 (2023): 555, https://doi.org/10.3390/ph16040555.

69. A. Daina, O. Michielin, and V. Zoete, "SwissTargetPrediction: Updated Data and New Features for Efficient Prediction of Protein

Targets of Small Molecules," *Nucleic Acids Research* 47 (2019): W357–W3664, https://doi.org/10.1093/nar/gkz382.

70. E. Orellana and A. Kasinski, "Sulforhodamine B (SRB) Assay in Cell Culture to Investigate Cell Proliferation," *Bio-Protocol* 6, no. 21 (2016): e1984, https://doi.org/10.21769/bioprotoc.1984.

71. M. Bursch, J.-M. Mewes, A. Hansen, and S. Grimme, "Best-Practice DFT Protocols for Basic Molecular Computational Chemistry," *Angewandte Chemie International Edition* 61, no. 42 (2022): e202205735, https://doi.org/10.1002/anie.202205735.

72. F. Feixas, E. Matito, M. Solà, and J. Poater, "Patterns of π-Electron Delocalization in Aromatic and Antiaromatic Organic Compounds in the Light of Hückel's 4n + 2 Rule," *Physical Chemistry Chemical Physics* 12, no. 26 (2010): 7126, https://doi.org/10.1039/b924972a.

73. R. Pucci and G. G. N. Angilella, "Density Functional Theory, Chemical Reactivity, and the Fukui Functions," *Foundations of Chemistry* 24 (2022): 59–71, https://doi.org/10.1007/s10698-022-09416-z.

74. J. Yu, N. Q. Su, and W. Yang, "Describing Chemical Reactivity With Frontier Molecular Orbitalets," *JACS Au* 2 (2022): 1383–1394, https://doi.org/10.1021/jacsau.2c00085.

75. G. Jhaa, P. D. Pancharatna, and M. M. Balakrishnarajan, "Topological Impact of Delocalization on the Stability and Band Gap of Partially Oxidized Graphene," *ACS Omega* 8, no. 5 (2023): 5124–5135, https://doi.org/10.1021/acsomega.2c08169.

76. P. M. A. Mekoung, B. Y. G. Mountessou, M. B. Mbah, et al., "Vibrational Spectroscopic Investigations, Electronic Properties, Molecular Structure and Quantum Mechanical Study of an Antifolate Drug: Pyrimethamine," *Computational Chemistry* 10 (2022): 157–185, https://doi.org/10.4236/cc.2022.104008.

77. *CCCBDB Listing of Precalculated Vibrational Scaling Factors*, accessed June 2, 2024, https://cccbdb.nist.gov/vibscalejust.asp.

78. C. M. Lee, J. D. Kubicki, B. Fan, L. Zhong, M. C. Jarvis, and S. H. Kim, "Hydrogen-Bonding Network and OH Stretch Vibration of Cellulose: Comparison of Computational Modeling With Polarized IR and SFG Spectra," *Journal of Physical Chemistry. B* 119 (2015): 15138–15149, https://doi.org/10.1021/acs.jpcb.5b08015.

79. G. M. Florio, T. S. Zwier, E. M. Myshakin, K. D. Jordan, and E. L. Sibert, "Theoretical Modeling of the OH Stretch Infrared Spectrum of Carboxylic Acid Dimers Based on First-Principles Anharmonic Couplings," *Journal of Chemical Physics* 118 (2003): 1735–1746, https://doi.org/10.1063/1.1530573.

80. M. Nasrollahzadeh, M. Atarod, M. Sajjadi, S. M. Sajadi, and Z. Issaabadi, "Plant-Mediated Green Synthesis of Nanostructures: Mechanisms, Characterization, and Applications," *Interface Science and Technology* 28 (2019): 199–322, https://doi.org/10.1016/B978-0-12-813586-0.00006-7.

81. M. Abdolkarimi-Mahabadi, A. Bayat, and A. Mohammadi, "Use of UV-Vis Spectrophotometry for Characterization of Carbon Nanostructures: A Review," *Theoretical and Experimental Chemistry* 57 (2021): 191–198, https://doi.org/10.1007/s11237-021-09687-1.

82. E. A. Arsenault, A. J. Schile, D. T. Limmer, and G. R. Fleming, "Vibronic Coupling in Energy Transfer Dynamics and Two-Dimensional Electronic-Vibrational Spectra," *Journal of Chemical Physics* 155, no. 5 (2021): 054201-1–054201-13, https://doi.org/10.1063/5.0056477/200959.

83. F.-F. Kong, X.-J. Tian, Y. Zhang, et al., "Probing Intramolecular Vibronic Coupling Through Vibronic-State Imaging," *Nature Communications* 12, no. 1 (2021): 1280, https://doi.org/10.1038/s41467-021-21571-z.

84. X. Chen, H. Li, L. Tian, Q. Li, J. Luo, and Y. Zhang, "Analysis of the Physicochemical Properties of Acaricides Based on Lipinski's Rule of Five," *Journal of Computational Biology* 27, no. 9 (2020): 1397–1406, https://doi.org/10.1089/cmb.2019.0323.

85. C. A. Lipinski, F. Lombardo, B. W. Dominy, and P. J. Feeney, "Experimental and Computational Approaches to Estimate Solubility and Permeability in Drug Discovery and Development Settings," *Advanced Drug Delivery Reviews* 46 (2001): 3–26, https://doi.org/10.1016/S0169-409X(00)00129-0.

86. C. M. Chagas, S. Moss, and L. Alisaraie, "Drug Metabolites and Their Effects on the Development of Adverse Reactions: Revisiting Lipinski's Rule of Five," *International Journal of Pharmaceutics* 549 (2018): 133–149, https://doi.org/10.1016/j.ijpharm.2018.07.046.

87. H. Pajouhesh and G. R. Lenz, "Medicinal Chemical Properties of Successful Central Nervous System Drugs," *NeuroRx* 2 (2005): 541–553, https://doi.org/10.1602/neurorx.2.4.541.

88. A. Zerroug, S. Belaidi, I. BenBrahim, L. Sinha, and S. Chtita, "Virtual Screening in Drug-Likeness and Structure/Activity Relationship of Pyridazine Derivatives as Anti-Alzheimer Drugs," *Journal of King Saud University, Science* 31 (2019): 595–601, https://doi.org/10.1016/j.jksus.2018.03.024.

89. R. O. Potts and R. H. Guy, "Predicting Skin Permeability," *Pharmaceutical Research* 9, no. 5 (1992): 663–669, https://doi.org/10.1023/A:1015810312465.

90. Y. C. A. Martin, "Bioavailability Score," *Journal of Medicinal Chemistry* 48, no. 9 (2005): 3164–3170, https://doi.org/10.1021/jm0492002.

91. N. Martinez Naya, J. Kelly, G. Corna, et al., "An Overview of Cannabidiol as a Multifunctional Drug: Pharmacokinetics and Cellular Effects. Molecules," 29, no. 2 (2024): 473, https://doi.org/10.3390/MOLECULES29020473.

92. Y. Lin, X. Sun, D. S. Su, G. Centi, and S. Perathoner, "Catalysis by Hybrid Sp2/Sp3 Nanodiamonds and Their Role in the Design of Advanced Nanocarbon Materials," *Chemical Society Reviews* 47, no. 22 (2018): 8438–8473, https://doi.org/10.1039/C8CS00684A.

93. P. R. Magalhães, P. B. P. S. Reis, D. Vila-Viçosa, M. Machuqueiro, and B. L. Victor, "Identification of Pan-Assay INterference CompoundS (PAINS) Using an MD-Based Protocol," *Methods in Molecular Biology* 2315 (2021): 263–271, https://doi.org/10.1007/978-1-0716-1468-6_15.

94. D. Gfeller, O. Michielin, and V. Zoete, "Shaping the Interaction Landscape of Bioactive Molecules," *Bioinformatics* 29, no. 23 (2013): 3073–3079, https://doi.org/10.1093/bioinformatics/btt540.

95. S. P. H. Alexander, "Common Receptors for Endocannabinoid-Like Mediators and Plant Cannabinoids," in *The Endocannabinoidome: The World of Endocannabinoids and Related Mediators* (Elsevier, 2015), 153–175, https://doi.org/10.1016/B978-0-12-420126-2.00010-9.

96. P. Morales and P. H. Reggio, "An Update on Non-CB 1, Non-CB 2 Cannabinoid Related G-Protein-Coupled Receptors," *Cannabis and Cannabinoid Research* 2 (2017): 265–273, https://doi.org/10.1089/can.2017.0036.

97. R. G. Pertwee, "Targeting the Endocannabinoid System With Cannabinoid Receptor Agonists: Pharmacological Strategies and Therapeutic Possibilities," *Philosophical Transactions of the Royal Society of London. Series B, Biological Sciences* 367 (2012): 3353–3363, https://doi.org/10.1098/rstb.2011.0381.

98. B. Kis, F. C. Ifrim, V. Buda, et al., "Cannabidiol—From Plant to Human Body: A Promising Bioactive Molecule With Multi-Target Effects in Cancer," *International Journal of Molecular Sciences* 20 (2019): 5905, https://doi.org/10.3390/ijms20235905.

99. E. Yuriev and P. A. Ramsland, "Latest Developments in Molecular Docking: 2010–2011 in Review," *Journal of Molecular Recognition* 26 (2013): 215–239, https://doi.org/10.1002/jmr.2266.

100. D. Ramírez and J. Caballero, "Is It Reliable to Take the Molecular Docking Top Scoring Position as the Best Solution Without Considering Available Structural Data?," *Molecules* 23, no. 5 (2018): 1038, https://doi.org/10.3390/molecules23051038.

101. T. Hua, K. Vemuri, M. Pu, et al., "Crystal Structure of the Human Cannabinoid Receptor CB1," *Cell* 167, no. 3 (2016): 750–762, https://doi.org/10.1016/j.cell.2016.10.004.

102. B. L. F. Kaplan, "The Role of CB1 in Immune Modulation by Cannabinoids," *Pharmacology & Therapeutics* 137 (2013): 365–374, https://doi.org/10.1016/j.pharmthera.2012.12.004.

103. X. Li, T. Hua, K. Vemuri, et al., "Crystal Structure of the Human Cannabinoid Receptor CB2," *Cell* 176, no. 3 (2019): 459–467.e13, https://doi.org/10.1016/j.cell.2018.12.011.

104. N. W. Choong and E. E. W. Cohen, "Epidermal Growth Factor Receptor Directed Therapy in Head and Neck Cancer," *Critical Reviews in Oncology/Hematology* 57 (2006): 25–43, https://doi.org/10.1016/j.critrevonc.2005.06.002.

105. L. Chin, A. Tam, J. Pomerantz, et al., "Essential Role for Oncogenic Ras in Tumour Maintenance," *Nature* 400 (1999): 468–472, https://doi.org/10.1038/22788.

106. A. M. Bode and Z. Dong, "Post-Translational Modification of P53 in Tumorigenesis," *Nature Reviews. Cancer* 4 (2004): 793–805, https://doi.org/10.1038/nrc1455.

107. R. A. Friesner, R. B. Murphy, M. P. Repasky, et al., "Extra Precision Glide: Docking and Scoring Incorporating a Model of Hydrophobic Enclosure for Protein-Ligand Complexes," *Journal of Medicinal Chemistry* 49 (2006): 6177–6196, https://doi.org/10.1021/jm051256o.

108. A. K. Tiwari, V. S. Rathore, D. Sinha, et al., "Design and Docking Studies of [Diethylenetriaminepentaacetic Acid–(Amino Acid)$_2$] With Acetylcholine Receptor as a Molecular Imaging Agent for Single-Photon Emission Computed Tomographic Application," *Molecular Imaging* 11, no. 3 (2012), https://doi.org/10.2310/7290.2011.00044.

109. M. L. Casanova, C. Blázquez, J. Martínez-Palacio, et al., "Inhibition of Skin Tumor Growth and Angiogenesis In Vivo by Activation of Cannabinoid Receptors," *Journal of Clinical Investigation* 111, no. 1 (2003): 43–50, https://doi.org/10.1172/jci200316116.

110. D. L. Lynch and P. H. Reggio, "Cannabinoid CB1 Receptor Recognition of Endocannabinoids via the Lipid Bilayer: Molecular Dynamics Simulations of CB1 Transmembrane Helix 6 and Anandamide in a Phospholipid Bilayer," *Journal of Computer-Aided Molecular Design* 20 (2006): 495–509, https://doi.org/10.1007/s10822-006-9068-9.

111. Y. Pei, R. W. Mercier, J. K. Anday, et al., "Ligand-Binding Architecture of Human CB2 Cannabinoid Receptor: Evidence for Receptor Subtype-Specific Binding Motif and Modeling GPCR Activation," *Chemistry & Biology* 15 (2008): 1207–1219, https://doi.org/10.1016/j.chembiol.2008.10.011.

112. F. Shahbazi, V. Grandi, A. Banerjee, and J. F. Trant, "Cannabinoids and Cannabinoid Receptors: The Story So Far," *iScience* 23 (2020): 101301, https://doi.org/10.1016/j.isci.2020.101301.

113. M. Arnittali, A. N. Rissanou, and V. Harmandaris, "Structure of Biomolecules Through Molecular Dynamics Simulations," *Procedia Computer Science* 156 (2019): 69–78, https://doi.org/10.1016/j.procs.2019.08.181.

114. A. Ligresti, A. S. Moriello, K. Starowicz, et al., "Antitumor Activity of Plant Cannabinoids With Emphasis on the Effect of Cannabidiol on Human Breast Carcinoma," *Journal of Pharmacology and Experimental Therapeutics* 318 (2006): 1375–1387, https://doi.org/10.1124/jpet.106.105247.

115. S. T. Lukhele and L. R. Motadi, "Cannabidiol Rather Than *Cannabis sativa* Extracts Inhibit Cell Growth and Induce Apoptosis in Cervical Cancer Cells," *BMC Complementary and Alternative Medicine* 16, no. 1 (2016): 335, https://doi.org/10.1186/s12906-016-1280-0.

116. L. De Petrocellis, A. Ligresti, A. Schiano Moriello, et al., "Non-THC Cannabinoids Inhibit Prostate Carcinoma Growth In Vitro and In Vivo: Pro-Apoptotic Effects and Underlying Mechanisms," *British Journal of Pharmacology* 168 (2013): 79–102, https://doi.org/10.1111/j.1476-5381.2012.02027.x.

117. W. H. Choi, H. Do Park, S. H. Baek, J. P. Chu, M. H. Kang, and Y. J. Mi, "Cannabidiol Induces Cytotoxicity and Cell Death via Apoptotic Pathway in Cancer Cell Lines," *Biomolecules & Therapeutics (Seoul)* 16 (2008): 87–94, https://doi.org/10.4062/biomolther.2008.16.2.087.

118. A. I. Fraguas-Sánchez, C. Martín-Sabroso, and A. I. Torres-Suárez, "Insights Into the Effects of the Endocannabinoid System in Cancer: A Review," *British Journal of Pharmacology* 175, no. 13 (2018): 2566–2580, https://doi.org/10.1111/bph.14331.

119. A. Preet, Z. Qamri, M. W. Nasser, et al., "Cannabinoid Receptors, CB1 and CB2, as Novel Targets for Inhibition of Non-Small Cell Lung Cancer Growth and Metastasis," *Cancer Prevention Research (Philadelphia, Pa.)* 4, no. 1 (2011): 65–75, https://doi.org/10.1158/1940-6207.capr-10-0181.

120. N. Martinez Naya, J. Kelly, G. Corna, M. Golino, A. Abbate, and S. Toldo, "Molecular and Cellular Mechanisms of Action of Cannabidiol," *Molecules* 28, no. 16 (2023): 1–24, https://doi.org/10.3390/molecules28165980.

121. C. Laezza, C. Pagano, G. Navarra, et al., "The Endocannabinoid System: A Target for Cancer Treatment," *International Journal of Molecular Sciences* 21 (2020): 747, https://doi.org/10.3390/ijms21030747.

Supporting Information

Additional supporting information can be found online in the Supporting Information section. **Data S1:** qua70172-sup-0001-supinfo.docx.